

Contourites and bottom current reworked sands: bed facies model and implications

de Castro, S.^{1,*} Sandra.deCastroSantos.2017@live.rhul.ac.uk., Hernández-Molina, F.J.¹, Rodríguez-Tovar, F.J.², Llave, E.³, Ng, Z.L.¹, Nishida, N.⁴, Mena, A.⁵

¹Dept. Earth Sciences, Royal Holloway Univ. London, Egham, Surrey TW20 0EX, United Kingdom

²Departamento de Estratigrafía y Paleontología, Universidad de Granada, 18002 Granada, Spain

³Instituto Geológico y Minero de España, 28003 Madrid, Spain

⁴Department of Environmental Sciences, Tokyo Gakugei University.Koganei, Tokyo 184-8501, Japan

⁵Departamento de Xeociencias Mariñas e Ordenación do Territorio, University of Vigo, Vigo, Spain

*Corresponding author.

Abstract

The differentiation of pure turbidites and contourites from mixed deposits —as the bottom current reworked sands (BCRS) — in sedimentary cores and outcrops from the modern or ancient records is still challenging. An accurate evaluation of facies associations calls for detailed understanding of processes controlling these deep-water systems and how they record interactions of along- and down-slope processes. Connecting features to processes is of particular relevance in the study of contouritic drifts that include sandy deposits. This research describes and interprets BCRS within a Pleistocene contouritic drift located along the middle continental slope of the Gulf of Cadiz. Seismic, wireline, and sedimentological analyses of sediment samples were applied to core material representing a muddy drift that hosts sandy deposits. A sedimentary sequence, comprising five facies (F1 to F5) is defined here; it records background sedimentation influenced by the initial deposition of a gravity-driven flow followed by bottom current reworking. It is moderately bioturbated and contains distinctive trace fossil assemblages, often dominated by ichnofabrics of the *Planolites* and *Thalassinoides*. These assemblages represent intermittent deposition between down-slope and along-slope processes during relatively short time scales. The sequence is defined as a partial bi-gradational contourite sequence including BCRS reworked from underlying turbiditic deposits due to the interaction of down- and along-slope processes within the contouritic drift and its adjacent contouritic channel. Longer-term trends include an increase and subsequent decrease in both sediment supply and bottom currents. The sedimentary facies model presented here represents a new end member for a mixed turbiditic-contouritic system in which turbiditic flows influence a contourite drift. As such, it may support basic sedimentological interpretation and petroleum exploration strategies.

Keywords: Mixed-systems, turbidites, contourites, reworking, deep-water, continental slope, Gulf of Cadiz

1. Introduction

A current problem in deep-water environments is the uncertain relationship between different processes that determine sedimentary stacking patterns in continental margins. Sediment gravity flows through submarine canyons and deep-water channels are traditionally considered the primary sediment transport processes connecting shallow- and deep-water environments (e.g., Lowe, 1982; Mutti, 1992; Meiburg and Kneller, 2010; Talling et al., 2012; Azpiroz-Zabala et al., 2017). The turbulent suspension cloud generated by flow-stripping and overspill can capture large volumes of fine-grained sediment in inter-canyon environments,

eventually settling along continental margins (Peakall et al., 2000; Prather, 2003; Kane et al., 2010; Hansen et al., 2015). Margins with a complex physiography —intra-slope basins, terraces, and scarps generated by tectonic activity (Pratson and Haxby, 1996) — can modify the behaviour of the gravity flow. Researchers now acknowledge the role of bottom (contour) currents in modifying or obliterating gravity flows. Some characteristics suggest that turbidity deposits can be affected by along-slope bottom currents (Sansom et al., 2018; Miramontes et al., 2020; Fonesu et al., 2020; Fuhrman et al., 2020). Vigorous bottom currents can rework previously deposited sediments, winnowing the seafloor and causing hiatuses and/or hardgrounds in the sediment record (Faugères et al., 1999; Hernandez-Molina et al., 2008; Stow and Smillie, 2020). They can also generate large erosional or depositional features that strongly influence the margin's sedimentary stacking pattern (Debevero et al., 2014).

During the 1960s, Heezen and Hollister (1964), Hsü (1964), and Hubert (1964) documented the importance of contouritic processes in the redistribution of down-slope (gravity-driven) deposits along continental slopes. Later studies showed that these processes were equally or locally, more significant than gravity flows in transporting, depositing, and reworking sediment (Faugères et al., 1999; Gonthier et al., 2003; Viana et al., 2007; Mulder et al., 2008; Mutti and Carminatti, 2012; Shanmugam, 2012, 2013). The interplay between along- and down-slope processes has been found to generate mixed turbiditic-contouritic depositional systems (Mutti et al., 1990; Mutti, 1990; Faugères and Stow, 2008; Hernández-Molina et al., 2008; Mulder et al., 2008; Brackenridge et al., 2010; Palamenghi et al., 2015; Creaser et al., 2017; Sansom, 2018; Fonesu et al., 2020; Fuhrman et al., 2020). This interaction promotes the deposition of well-sorted sands through reworking of overspill sediments in intra-canyon areas (Stanley, 1988, 1993; Shanmugam et al., 1993). Although the continuum may be dominated by either along- or down-slope processes, but the full range of their resulting sedimentary facies is not known. A variety of sedimentary facies with attributes related to gravity and contouritic processes may be involved (Stanley, 1988; Hüeneke and Stow, 2008; Mulder et al., 2008; Fonesu et al., 2020; Fuhrman et al., 2020). Recent studies propose mixed systems based on sedimentary and seismic stratigraphic features (Sansom, 2018; Fonesu et al., 2020; Fuhrman et al., 2020) or ichnological ones (Rodríguez-Tovar and Hernández-Molina, 2018; Dorador et al., 2019; Míguez-Salas and Rodríguez-Tovar, 2019; Rodríguez-Tovar et al., 2019a, b). Because of their role in deep-water petroleum plays, interest in these mixed system has peaked (e.g., Viana, 2008; Sansom, 2018; Fonesu et al., 2020).

In classic contourite drifts, thick, fine-grained (muddy) deposits may act as seal rocks (Viana, 2008). Sandy deposits along contourite channels, moats, and contourite terraces, in

lateral association with drifts, may serve as potential reservoirs (Viana et al., 2007; Viana, 2008; Mutti et al., 2014; Hernández-Molina et al., 2016a). Yet the provenance of these deposits and their lateral and vertical links with contourite channels and drifts remain uncertain. Current facies models do not address the role of gravity (turbiditic) processes in building or modifying large contouritic features.

The Gulf of Cadiz is an excellent site for studying the interaction between along- and down-slope sedimentary processes and associated facies. This continental margin hosts a contourite depositional system (CDS) along the middle slope that evolved through local interactions with down-slope processes since the early Pliocene (Llave et al., 2007, 2019; Hernández-Molina et al., 2008, 2016b; García et al., 2009; Roque et al., 2012). The aims of the present study are: a) to identify contourite and bottom-current reworked sand deposits within this CDS and characterise their sedimentary facies, b) to evaluate the role of turbidites in contourite drift formation and present a sedimentary sequence model, and c) to briefly consider conceptual and economic implications.

2. Regional setting

2.1. Geological and morphosedimentary framework

The Gulf of Cadiz represents the boundary between the African and Iberian plates in the Atlantic, at the westernmost edge of the Alpine-Mediterranean orogenic belt. Its tectonic history includes phases of extension, convergence, and strike-slip motion related to successive phases of the opening of the North Atlantic, closure of the Tethys ocean, and the subsequent opening of the western Mediterranean basins (Maldonado et al., 1999). The westward drift and collision of the Alboran Domain with the North African and South Iberian margins, during the early to middle Miocene, led to the Betic–Rif orogeny and associated Neogene basins. Westward roll-back subduction of an oceanic lithosphere slab beneath the Gibraltar Arc took place during the late Miocene (Tortonian); its accretionary wedge during emplaced massive bodies of allochthonous materials referred to as the olistostrome unit (Maldonado et al., 1999; Terrinha et al., 2009; Duarte et al., 2013) or the allochthonous unit of the Gulf of Cadiz (AUGC; Medialdea et al., 2004). They record the propagation of the Mediterranean Alpine collision belt into the Atlantic. Triassic and mid-Miocene marls of the AUGC and salts penetrate overlying sediments in the Gulf of Cadiz to form diapiric ridges and adjacent depocenters (Maldonado et al., 1999; Llave et al., 2007; Medialdea et al., 2009).

The northern continental margin of the Gulf of Cadiz is 350 km long and runs from the Strait of Gibraltar northwards to Cape St Vincent on the SW coast of Portugal (Fig. 1A). The

continental slope along this margin comprises three physiographic domains (Fig. 1A): 1) a moderately steep (2° – 3°) upper slope at a water depth 150 and 400 m, 2) two gently dipping ($>1^{\circ}$), wide terraces located along the middle slope at 500–750 m and 800–1200 m water depth, and 3) a very gradual (1° – 0.5°) lower slope (Hernández-Molina et al., 2003). The Gulf of Cadiz CDS occurs along the middle slope and consists of five major morphosedimentary sectors. They include (Fig. 1A): 1) a proximal scour and sand-ribbons sector, 2) an overflow-sedimentary lobe sector, 3) a channels and ridges sector, 4) a contourite deposition sector, and 5) a submarine canyon sector (Hernández-Molina et al., 2003, 2006; Llave et al., 2007). This study focuses on morphosedimentary sectors 1 and 3 (proximal and distal sectors respect to the Strait of Gibraltar respectively), which lie within a contourite terrace. They were drilled by the Integrated Ocean Drilling Program (IODP) Expedition 339 (Stow et al., 2013b; Hernández-Molina et al., 2016b) (Fig. 1A). Site U1388 is located in the proximal sector 1 near the Strait of Gibraltar (Fig. 1B) and consists of a thick (~815 m) sandy sheeted drift with sand layers averaging 12–15 m in thickness (Nelson et al., 1993; Buitrago et al., 2001). Site U1389 is located in the central part of sector 5, in the Huelva mounded drift (Figs. 1B and 2A). This locality has complex depositional and erosional contouritic features developed since the late Pliocene (Hernández-Molina et al., 2016b). The drift developed between the Huelva channel (3.5 km to the north) and the Guadalquivir channel (4.4 km to the south). Sector 3 hosts three NE-trending tectonic ridges: the Doñana, Guadalquivir, and Cadiz ridges (Fig. 1B). These ridges were reactivated by growth faults in the Pliocene and Quaternary, giving rise to discontinuities and hiatuses evident in the sedimentary record. Previous work provides details of the Pliocene to Quaternary history of the Gulf of Cadiz, including sectors 1 and 3 (Llave et al., 2007; Roque et al., 2012; Hernández-Molina et al., 2016b; Lofi et al., 2016).

2.2. Oceanographic framework

The modern hydrographic regime of the Gulf of Cadiz is dominated by an exchange of water masses between the Atlantic Ocean and the Mediterranean Sea (Ochoa and Bray, 1991; Bryden et al., 1994). The Strait of Gibraltar acts as a gateway that allows westward bottom flow of the warm and highly saline Mediterranean Outflow Water (MOW) and eastward input of the overriding turbulent, less saline, and cold North Atlantic Surface Water (NASW) into the Mediterranean Sea (Ambar and Howe, 1979; Baringer and Price, 1999). The MOW accelerates in this confined gateway, reaching velocities near 300 cm/s (Ambar and Howe, 1979; Mulder et al., 2003). After exiting the Strait of Gibraltar, the MOW moves northwest

along the Gulf of Cadiz's middle continental slope (400 and 1200 m water depth) and divides into two main cores. The upper core or Mediterranean upper water (MU) flows along the base of the upper slope at 400 to 800 m water depth, whereas the lower core or Mediterranean lower water (ML) flows between 800 and 1200 m water depth. Recent studies establish a more complex structure for the MOW, entailing up to five different branches (M1 to M5), the most surficial branch M5 being equivalent to the MU (Sánchez-Leal et al., 2017). The MU constitutes at the present day the principal core in the upper-to-middle slope transition; it flows northwestwards at an average velocity of $0.2 - 0.5 \text{ m s}^{-1}$ (Kenyon and Belderson 1973; Ochoa and Bray 1991; Hernández-Molina et al., 2003, 2006; Sánchez-Leal et al., 2017). The MOW circulation in the Gulf of Cadiz is influenced by the complex local topography, which accelerates the flow in certain areas (Sánchez-Leal et al., 2017). It divides into five distinct branches: the Southern Branch, the Northern Branch, the Central Branch, the Eastern Branch, and the Western Branch (Fig. 1B) (García et al., 2009).

3. Dataset and methods

A variety of datasets were used to analyse sedimentary sequences at different spatial scales.

3.1. Large-scale features

Seismic data

Multichannel seismic profiles (MCS) were used to identify the main seismic units, the physiographic setting, and features indicative of depositional or erosional processes. MCS were acquired on different academic and industry projects and cruises (HE-91-3, PD00 and S81, Fig. 1C), and data were processed using stacking and time migration methods (see details in Maldonado et al., 1999 and Brackenridge et al., 2013). Seismic analysis of seismic units and facies entailed conventional methods and criteria described in Mitchum et al. (1977) and Catuneanu et al. (2009). Our analysis focused on the central sector of the CDS, around IODP Expedition 339 Site U1389. Surface (isochrone) maps were derived for regional paleogeographic reconstruction. They were generated with a grid increment of 50 m in both directions, without smoothing processes.

3.2. Medium-scale features

Wireline logs

Downhole well logs from the IODP sites were acquired using the triple combo of Schlumberger logging tools (resistivity, density, and natural gamma-ray) at Sites U1389A and U1389E (Expedition 339 Scientists, 2012; Stow et al., 2013b). Log data in Holes U1389A and U1389E cover a common interval between 100 and 350 mbsf. Downhole measurements were made in Hole U1389A to a total depth of 354.9 mbsf, and 567 mbsf in Hole U1389E (Stow et al., 2013; Hernández-Molina et al., 2016b). We studied Hole U1389E gamma-ray logging as it reached the top of the Q4 subunit. For further information of drilling procedures see Stow et al. (2013b). Only considered gamma-ray logs were considered here to determine lithological changes; they were acquired with a sampling resolution of 15.24 cm and an approximate vertical resolution of 20–30 cm. The gamma-ray dataset from Hole U1389E was compared to grain-size data obtained from Site U1389A core material. Vertical seismic profiles (VSP) relating borehole depth to travel time in seismic reflection data were correlated with regional multichannel seismic profiles (further information in Hernández-Molina et al., 2016b).

3.3. Small-scale features

Core data and chronological framework

Cores from two boreholes drilled during the IODP Expedition 339 in the Gulf of Cadiz were analysed—Site U1388 (36°16.142'N; 6°47.648'W at 350 m water depth) located in the Northern Contourite Channel, and Site U1389 (36°25.515'N, 7°16.683'W at 644 m water depth) located on the Huelva rounded drift (Expedition 339 Scientists, 2012; Stow et al., 2013b). Eight cores were obtained, five (Holes A-E) from Site U1389 and three (Holes A-C) from Site U1388 (Table 1).

Sedimentary analysis focused on the cores from Holes U1389A, U1389C, and U1388B. High-resolution core imaging was performed for analysis of lithology, colour, bed boundaries, sedimentary structures, and ichnological features. As the sandier intervals had less consolidated sediment, wash-out during drilling may bias results for these intervals. Chronological constraints were derived from biostratigraphic analysis and interpretation of IODP Expedition 339 (Expedition 339 Scientists, 2012; Stow et al., 2013b). Sedimentary facies and their associations were interpreted in view of colour, texture analysis, microfacies, sedimentary structures, X-Ray Fluorescence (XRF), and Scanning Electron Microscopy (SEM) results.

Textural analysis

Grain size analysis included 2667 splits of core material from Holes U1389A as sampled at 25 cm intervals. A total of 58 samples were collected to increase the resolution for some sedimentary sequences. Grain size analysis was performed at the University of Bordeaux, EPOC laboratory (France), using a Malvern Mastersizer S laser microgranulometer. This device measured a grain size range of 0.02 to 2000 μm (clay to sand). A value of 1.33 was adopted as the particle refractive index. Grain size parameters were obtained from bulk sediment and analysed by means of Gradistat software, adopting its grain size scale (Blott and Pye, 2001). Mean grain size, sorting, skewness, and kurtosis were calculated using the method of Folk and Ward (1957). Results were compared by cross-plots (Folk, 1964; Martins, 2003).

Thin section analysis

One large-size (20 x 2cm) and 20 regular-size (4 x 1cm) thin sections were respectively obtained at the University of Greifswald (Germany) and Royal Holloway University of London (United Kingdom). Thin sections were used to document microfacies and small-scale sedimentary structures. Grain frequency was determined by visual comparison with charts from Baccelle and Bosellini (1965) and Mathew et al. (1991).

X-Ray Fluorescence (XRF)

XRF was conducted on well-preserved, intact sections spanning a total length of 7.5 m of the section (Table 1). Data were collected at 5 mm intervals using a XRF Core Scanner II (Avaatech Serial No. 2) at the MARUM laboratories of the University of Bremen (Germany). These scans covered a sample area of 12 cm² with a down-core slit size of 5 mm. Generator settings of 10/30 kV at 0.4 and 1 mA were analysed for 10 and 15 s (respectively) at the split core surface. The core surface was shielded by 4 μm thick SPEXCerti Prep Ultralene1 foil to avoid contamination of the XRF measurement unit and prevent desiccation of the sediment. The XRF data were acquired using a Canberra X-PIPS Silicon Drift Detector (SDD; Model SXD 15C-150-500) with 150 eV X-ray resolution, the Canberra Digital Spectrum Analyzer DAS 1000, and an Oxford Instruments 50W XTF5011 X-Ray tube with rhodium (Rh) target material. Raw spectra were processed using the Iterative Least square software (WIN AXIL) package from Canberra Eurisys. Points from disturbed intervals in the core face (i.e., fractures and cracks) were removed, and data were retained only from elements that gave consistently good signal quality (i.e., Al, Si, K, Ca, Ti, Fe, Sr, and Zr). These elements were standardised

according to mean values and standard deviations. Pearson correlation coefficients were calculated to identify significant relationships and element associations.

The cross-plots presented below show significant trends in chemical compositions according to sedimentary facies and depositional parameters. For example, $\ln \text{Zr/Al}$ is interpreted as an indicator of bottom current strength due to the accumulation of heavy minerals within the sediment (Bahr et al., 2014, 2015; Kaboth et al., 2016). Ratios of $\ln \text{Ca/Ti}$ can be used to detect variation in biogenic (Ca) and detrital (Ti) sediment supply (Hodell et al., 2013). Strong correlations between Ca and Sr support the use of $\ln \text{Ca/Sr}$ as a proxy for changes in carbonate (foraminifera/shallow-marine bioclast) assemblages (Thomson et al., 1999, 2004; Ritcher et al., 2006; Rothwell et al., 2006; Keul et al., 2017).

Scanning Electron Microscopy (SEM) observations

Microstructure analysis was used to identify fine-grained sediment structures in selected samples (Table 1) at the top and bottom of the sedimentary sequence. Vertically aligned samples were dried and embedded in 10 cm³ epoxy mounts. Samples were coated with an Au/Pd film using a sputter coater (JEOL Ion Coater JFC-1100) and imaged using SEM (Hitachi S-3400N) at the Tokyo Gakuai University (Japan). The three thin sections (Table 1) subjected to microtexture analysis were selected from sandy, quartz-bearing intervals. Glass microscope slides (50 x 26 mm) were ground and polished to 1200 μm thickness for sample mounting and gold film coating. Thin sections were then imaged using a Zeiss EVO MA15 at the Geology and Geochemistry Laboratories of Eni SpA in Milan (Italy).

Ichnological analysis

Ichnological analysis of core samples was conducted after digital enhancement of high-resolution images to increase visibility of biogenic structures, following the procedure followed described in Dorador et al. (2014a, 2014b), Dorador and Rodríguez-Tovar (2018), and Miguez-Salas et al. (2019). Orientation, shape, size, distribution, infilling material, and degree of bioturbation were recorded.

3.3. Nomenclature

The nomenclature adopted to describe the main seismic units and discontinuities is that outlined for the Pleistocene record of previous studies (e.g., Llave et al., 2007; Hernández-Molina et al., 2016b). These authors identified three main regional seismic units (QI, QII, and QIII) and six subunits (Q1 to Q6) bounded by three major regional discontinuities (Fig. 2A).

They feature an early Quaternary discontinuity (EQD), middle Pleistocene discontinuity (MPD), and late Quaternary discontinuity (LQD). Our research focussed on subunits Q4 and Q5. The description of log data follows the nomenclature of Serra and Sulpice (1975), which defines gamma-ray values and trends. The distribution of geological and sedimentary features based on the seismic data set published by Llave et al. (2007) and García et al. (2009) have provided the regional 3D framework for the considered palaeogeographic reconstruction on this work, that have been improved with our new results.

The term ‘contourites’ is used for sediments deposited or substantially reworked by the persistent action of bottom currents (Faugères and Stow, 2008; Rebesco et al., 2014). Thick, extensive contourite sediment accumulations are called contourite drifts. The criteria for drift morphologies and internal configurations are defined by Rebesco (2005) and Rebesco et al. (2014). Turbidity currents refer to gravity-driven currents in which the sediment is supported by the upward component of fluid turbulence (Middleton and Hampton, 1973; Dasgupta, 2003; Meiburg and Kneller, 2010; Mulder, 2011). Froiditic deposits denote sediments left by turbidity currents (Sanders, 1965; Middleton and Hampton, 1973; Lowe, 1982; Shanmugam 2000; Mutti et al., 2009; Talling et al., 2012; Mulder and Hüneke, 2014).

4. Results

4.1. Seismic stratigraphic analysis

The Q4 subunit is bounded at its base by an erosive, high-amplitude reflection that truncates the underlying deposits, referred to herein as the R4 discontinuity (Fig. 2A). The surface map for R4 shows three main depressions separated by the NE-trending Guadalquivir and Cadiz diapiric ridges. They are bound by the Betic front and flysch units to the east, and by the Guadalquivir bank to the west (Fig. 2B). Figure 2A shows the trough-fill configuration and aggradational stacking pattern found at the base of subunit Q4. Above these facies, the subunit exhibits high-amplitude, channelized, v-shaped features with an infill pattern of oblique-parallel and locally discontinuous reflections (Channel System I; Fig. 2A and 2D). These channelized features span 500 m in width and reside at 0.075 s TWT depth. Their steeply dipping walls show truncations and eastward migration patterns. The top of subunit Q4 has additional, continuous, subparallel reflections that are particularly evident in the basin centre (Fig. 2A and 2D). Towards the ENE, at the basin margin, the subunit displays complex, oblique seismic reflections that downlap in a basinward direction against previous deposits (Fig. 2E).

The Q5 subunit is bound by the regional MPD and LQD. The MPD is a basal boundary seen as a high-amplitude reflection marking an erosional truncation surface (Fig. 2A). Reflections onlap above the MPD both along the basin margin and within diapiric ridges, but coincide with the MPD in basin centres (Fig. 2A). The surface map for the MPD (Fig. 2C) has features similar to the R4 (Fig. 2B), including the four main depressions separated by the Guadalquivir and Cadiz diapiric ridges (Fig. 2C). The two surface maps diverge in showing the Cadiz diapiric ridge as a linear feature (MPD surface map), while the Guadalquivir diapiric ridge appears as a segmented and discontinuous feature sharing the northeasterly trend. Depressions also show less incision (0.9 s TWT deep) but maintain the same northeasterly trend (Fig. 2C). Subunit Q5 exhibits an aggradational internal configuration with parallel, continuous high-amplitude reflections. They have a sheeted external expression in the central part of the basin. Laterally, it shows channel-fill configurations (Channel System II) are found towards the Guadalquivir ridge, to the ENE, between the Huelva mounded drift and the Huelva contourite channel (Fig. 2A). This area harbours two channelized packages with u-shaped features that truncate underlying units (Fig. 2E). These features are symmetric: a wide, flat base, and gently dipping walls. They span 3 km in width and occur at depths of 0.125 s TWT. They show erosional features plus a continuous, high-amplitude reflection at their base. They contain parallel, continuous, high-amplitude seismic reflections in basal areas that transition into less continuous, low-amplitude reflections toward the upper surface (Fig. 2E). The high-amplitude basal reflections extend laterally along the Huelva mounded drift. Low-amplitude reflections at the upper surface have oblique trends and end abruptly on either sides of the u-shaped feature (Fig. 2E); they match the facies observed laterally towards the Huelva mounded drift (Fig. 2E). The LQD would be the upper boundary of this subunit and appears as a high-amplitude reflection (Fig. 2A and 2E).

4.2. Well-logging gamma-ray trend analysis

The well-logging analysed in this study, from 220 to 355 m below sea floor (mbsf), runs from the top of subunit Q4 up through two-thirds of subunit Q5 (Fig. 3). Gamma-ray values for this interval range between 20 and 70 API units, indicating shifts from sand- to silt-deposits (Fig. 3). Two types of gamma-ray log trend can be discerned (Fig. 3). First, a serrated one of fluctuating gamma-ray values occurs over a 69 m thick interval, from 294 to 363 mbsf (Fig. 3). The MPD discontinuity appears within this gamma-ray trend at 318 mbsf as a spike in gamma-ray response (17.5 API). The second is a funnel-shaped trend with an upward decline in gamma-ray values between 444-394 and 294-215 mbsf.

4.3. Sedimentary facies analysis

Figure 3 presents grain size analysis for Q4 and Q5 sub-units. Nine sedimentary sequences were identified from Hole U1389A and three from Hole U1389C (Table 1). Moreover, five sedimentary sequences seen in coeval intervals from Hole U1388B (Table 1) were compared with those identified at Site U1389. The base of the lowermost sedimentary sequence occurs at 349.7 mbsf and the uppermost at 244.02 mbsf for Hole U1389A (Table 1). The uppermost sedimentary sequences (cores 27X and 28X) correspond to the funnel-shaped gamma-ray trend, while the other sequences signal the serrated trend (36X, 37X, 38X, and 39X) (Fig. 3). Correlation analysis of XRF results pointed to two main groups, serving as proxies for detrital (i.e., Fe, Zr, Ti, Al, K) versus carbonate input (Ca, Sr; Table 2). As summed up in Figure 4, the sedimentary sequences comprise five evidently different vertical facies evident from Sites U1389 and U1388.

4.3.1. Facies 1 (F1)

F1 consists of structureless, fine-grained, poorly-sorted silt ranging between 6.63 and 12.27 μm (Fig. 4). It commonly occurs below the base of the sandy deposits and reaches up to 12 m in thickness (Figs. 5, 6, 7A and 7B). Grain size distribution curves show clear differences between: 1) a unimodal distribution with a symmetric skew (Fig. 5A and 5B), and 2) a slightly bimodal platykurtic distribution that reflects mixing of a dominant fine silt fraction with less common sand and coarse silt (Fig. 5C, 5D and 5E). This facies gives the highest $\ln \text{Ca/Sr}$ values but does not exhibit major peaks in $\ln \text{Ca/Ti}$, $\ln \text{Zr/Al}$, or $\ln \text{Ca/Sr}$ (Fig. 5). Discrete traces are present (Fig. 6A-E) or absent (Fig. 6G) in F1. When present, *Thalassinoides* appears as isolated burrows below the upper contact with F2. These traces are infilled by sediment coarser than the host sediment (F1) and similar to that from the overlying facies (F2).

The F1 microfacies is dominated by a matrix-supported texture —80% matrix, 10% quartz grains, and about 10% bioclasts. Thin, irregular bands slightly enriched in silt define subtle, sub-horizontal laminations (Fig. 7A and 7B). SEM microstructure observations of F1 reveals two particle orientations: 1) calcareous nannoplankton and silt grains with plate grains parallel and subparallel to the bedding plane (Fig. 8A), and 2) calcareous nannoplankton, randomly-oriented clay particles having edge-to-face and edge-to-edge contacts, and silt grains with plate grains parallel or subparallel to the bedding plane (Fig. 8B).

4.3.2. Facies 2 (F2)

F2 consists of very poorly-sorted sediments with mean grain sizes from coarse silt to very fine sand, and ranging from 42.55 to 141.85 μm (Fig. 4). Beds of this massive or normally graded facies exhibit sharp bases with medium-grain shells fragments (Fig. 6E and 6G). The average sedimentary thickness of F2 is 2-3 cm in average sedimentary thickness (Fig. 6), but some intervals can reach up to 55 cm (e.g., Figs. 5A and 6E). The grain size frequency draws a bimodal coarse-skewed curve depicting very fine sand with a leptokurtic distribution, along with a lesser mud component showing platykurtic distribution (Fig. 5). Overall, F2 is relatively high in $\ln \text{Zr/Al}$ and $\ln \text{Ca/Sr}$ values (Fig. 5E). F2 contains just a few trace fossils, occurring as isolated *Planolites* (Fig. 6F and 6G) or as several burrows within a horizon (Fig. 6A).

The F2 microfacies has a matrix-supported texture made up of 50% matrix, 30% quartz grains, and 20% bioclasts (Fig. 7A and 7B). Grains show primarily angular to subrounded monocrystalline quartz, calcite fragments, bioclasts (mostly shallow-marine bivalve and equinoid fragments), and planktonic and benthic foraminifera. Intraclast occur at the base of the beds (Fig. 7B). The composition and colour of these mud-clasts resemble those of F1, which enables their differentiation from the surrounding F2 sediments.

4.3.3. Facies 3 (F3)

F3 consists of sub-horizontal laminated, poorly-sorted and very coarse silt to very fine sand, with a mean grain size ranging from 55.64 to 170.26 μm (Fig. 4). This facies shows both sharp and transitional bases and an average thickness of 4 cm (Fig. 6). The grain size distribution displays a bimodal coarse-skewed shape characterised by a leptokurtic distribution for the dominant sand component and a platykurtic distribution for the subordinate silt component (Fig. 6). F3 shows peaks in $\ln \text{Zr/Al}$ ratios, yet $\ln \text{Ca/Ti}$ and $\ln \text{Ca/Sr}$ ratios remain relatively constant (Fig. 5A and B). F3 shows only scarce bioturbation, with occasional horizons containing *Planolites* (Fig. 6A).

The F3 microfacies consists of discrete, alternating matrix- and grain-supported laminae (Fig. 5). The matrix content of F3 is relatively lower (around 20%) than that of F1 and F2 (Fig. 7A). The remaining sediment has 55% quartz grains—mostly of monocrystalline quartz and are subangular to rounded with poor to moderate texture—and 25% bioclasts. This facies shows uniform quartz grain size distributions throughout the interval, that is, no strong deviations among laminae. F1 mud chips are interbedded in the facies (Fig. 7A and 7C).

4.3.4. Facies 4 (F4)

F4 features moderately-sorted, very fine to fine-grained sands, with a mean grain size ranging from 87.50 to 179.55 μm (Fig. 4). This is the most distinctive facies recognised within the sedimentary sequences analysed. The gradual base of F4 exhibits thin, rhythmic alternations of coarse silts forming wavy to horizontal laminations, and fine sand with lenticular shapes and laminae inclined from about 5° to 20° . The average thickness is 5 to 10 cm (Fig. 6). Sandy lenses are typically less than 0.5 cm thick, but may measure up to 1 cm (Fig. 6B). The sand fraction has a largely unimodal frequency distribution, with a leptokurtic or even very leptokurtic distribution. It is also slightly skewed (Figs. 4 and 5). F4 shows no major peaks in $\ln \text{Ca/Ti}$, $\ln \text{Zr/Al}$, or $\ln \text{Ca/Sr}$. However, some samples exhibited three peaks in $\ln \text{Zr/Al}$ (Fig. 5D) or a slight increase in $\ln \text{Ca/Ti}$ (Fig. 5E) with stratigraphic position. F4 shows scarce bioturbation and contains *Planolites* as isolated burrows in horizons at 25 cm and 53.5 cm depth in the cores (from Fig. 6A and 6E, respectively).

The F4 microfacies contained the lowest matrix content (10%) along with 80% quartz grains and 10% bioclasts. It traces an inversely graded trend from its base to its upper surface (Fig. 5). Two interlaminar elements contain very fine grain-supported and very fine mud-supported sand. The grain-supported laminae are subrounded to angular, moderately to well sorted (Figs. 7A, 7D and 9A). The matrix-supported laminae consist primarily of subrounded to angular, moderately-sorted monocrystalline quartz grains. Discrete laminations within, or opaque concentrations, are greater near matrix-supported laminae than near grain-supported laminae (Figs. 7A and 9B-D). The contacts between matrix- and grain-supported laminae are either gradual at the base and top (Fig. 9B), sharp at the base and gradual at top (Fig. 9C), or sharp at both the base and top (Fig. 9D). SEM images evidence quartz grains surrounded by matrix in grain-supported laminae (Fig. 8C).

4.3.5. Facies 5 (F5)

F5 consists of normally graded, very poorly-sorted coarse silt to fine sand, its mean grain size ranging from 51.99 to 169.48 μm (Fig. 4). F5 shows a transitional basal contact (Fig. 7E). This facies reaches up to 1 m in sedimentary thickness, and transitions upward into F1 (Figs. 5 and 6). It exhibits a well-developed, mottled silt background and randomly distributed shell fragments, but no sedimentary structures (Fig. 6). The grain size distribution gives a bimodal coarse-skewed curve with a leptokurtic distribution for sand and a platykurtic distribution for the silt (Figs. 4 and 5). F5 has fairly homogeneous $\ln \text{Ca/Ti}$, $\ln \text{Zr/Al}$, and $\ln \text{Ca/Sr}$ ratios, though some core samples showed peaks in $\ln \text{Zr/Al}$ (Fig. 5B). F5 is highly

bioturbated and has abundant trace fossils, including both *Thalassinoides* and *Planolites*, which occur as isolated burrows (Figs. 6F and G) and in successive horizons (Fig. 6C).

F5 microfacies have a matrix-supported texture with 35% matrix, 30% quartz grains, and 35% bioclasts. Clasts include angular to subrounded monocrystalline quartz, calcite, and bioclasts often composed of planktonic foraminifera (Fig. 7E). This facies generally contains millimetric scale discrete laminations defined by concentrations of opaques (Fig. 7A). The SEM microstructure observed at the top of F5 consists of calcareous nannoplankton, randomly-oriented clay particles exhibiting edge-to-face and edge-to-edge contacts, and silt grains with plate grains oriented parallel and subparallel to the bedding plane (Fig. 8D).

4.4. Facies associations

The five identified facies form a vertically related sedimentary sequence wherein F1, F2, F3, F4, and F5 evolve upward again into F1. The sequence begins and ends with muddy sediments (F1) that bracket sandy deposits (F2 to F5). The transition from muddy (F1) to sandier deposits is abrupt in the lower part of the sequence (F1 to F2), but the transition from sandy to muddy sediments is gradual in the upper part (F5 to F1).

Figure 10 offers cross-plots of grain size distributions for each facies. Scatter-plots for F1 and F4 show a trend unlike that of other facies. Cross-plots of mean grain size versus kurtosis exhibit a clear trend from platykurtic (F2, F3, and F5) to very leptokurtic (F4) as grain size increases from coarse silt to fine sand (Fig. 10A). By contrast, F1 shows a mesokurtic distribution. The cross-plot of mean grain size against skewness indicates that medium to very fine sands (F2 to F5) deposits are generally skewed towards fine to very fine relative to F1, which contained the finest-grained sediment displaying a symmetrical skew (Fig. 10B). Cross-plots of mean grain size and sorting show a general decline in sediment sorting with increasing mean grain size. Yet, F4 does not show this trend, instead reflecting better sorting associated with an increase in fine sands (Fig. 10C). Cross-plots of skewness and sorting show three distinctive trends. Trend *a* applies to F1, trend *b* applies to most of F2 as well as F3, F4, and F5, and trend *c* applies to F4 and F3 (Fig. 11A). Trends *a* and *c* exhibit linear tendencies, while *b* lacks consistent behavior. The cross-plot showing skewness versus kurtosis likewise displays three trends: *a* applies to F1, *b* applies to F2 and F5, and *c* applies to F4. The F3 data points subtly delineate between trends *a* and *c* (Fig. 11B).

Figure 12 shows scatter plots of different XRF proxies. All facies follow the same broadly linear trend in terrigenous input (Fe/Ti) (Fig. 12A). The cloud of F1 data points does not overlap with those representing the facies that exhibit the highest Fe/Ti and Si/Ti values (Fig.

12A and 12B). Siliciclastic input (Si/Al) diverges for F3 and F4, both of which are comparatively enriched in Si (Fig. 12B). Carbonate input (Ca/Ti and Sr/Ti) cross-plots also point to diverse relationships among the facies. F1 does not overlap with the rest, and contrasts with F3 and F4 (Fig. 12C and 12D). The F2 and F5 data represent intermediate values in all cross-plots. The \ln Ca/Ti vs. \ln Zr/Al proxies exhibit three noteworthy trends (Fig. 12E). For F1 there is a relatively constant relation between the two proxies (*a*). Both F2 and F5 show a positive correlation between \ln Ca/Ti and \ln Zr/Al proxies (*b*), whereas F3 and F4 show a negative correlation (*c*). The \ln Ca/Sr vs. \ln Si/Al plot reflects the enrichment of foraminifers over shallow-marine bioclast with quartz grains (Si) upon matrix content (Al). This plot shows three main trends: F1; F2 and F5 having a negative correlation with Si and a positive correlation with Ca; and F3 and F4 with no correlation (Fig. 12F). Overall, these analyses support facies associations of F1, F2 and F5, in contrast with F3 and F4.

5. Interpretation

5.1. Large-scale interpretation: contourite drift and channel systems

At large scales, the aggrading subunits Q4 and Q5 constitute a contouritic drift developed by a relatively weak MOW. They also reveal complex interactions among drift deposits, lateral erosional features, and local structural features. The R4 surface map shows structural relief and diapiric ridges whose formation and development created numerous NE-SW trending valleys perpendicular to the margin (Fig. 2B). These channelized features are interpreted as marginal valleys on the lee side of linear diapiric ridges. Most valleys are abrupt, elongate, narrow channels running downslope, parallel to the western flanks of the ridges (García et al., 2009; Fernández-Molina et al., 2014; Lozano et al., 2020). The complex topography could exert a potential major influence on transport by confining sediment gravity flows (Kneller and Buckee, 2000), by developing Channel System I. The initiation of down-slope Channel System I began in the upper part of subunit Q4, coeval in time with the appearance of the marginal valleys (Fig. 2A and 2D). Channel system I consisted of downslope small canyons or gullies similar to those documented along other continental margins (Ercilla et al., 2008; Gales et al., 2013; Gong et al., 2015). These gullies evidence gravitational processes induced by tectonic and diapiric activity (Llave et al., 2007; Hernández-Molina et al., 2016b).

During the MPD, renewed of tectonic activity triggered the uplift and segmentation of the Guadalquivir and Doñana diapiric ridges. This led to the activation of Channel System II and a major shift in the MOW pathway and depositional setting, as proposed Llave et al. (2007).

Although the full establishment of the Channel System II can be linked to the MPD, the presence of oblique seismic reflections at the top part of subunit Q4, suggest a Channel System II drift transition (Fig. 2E) was already active, hence coeval with the downslope gullies (Channel System I) and marginal valleys. During deposition of subunit Q5, Channel System II formed the u-shaped channels (Fig. 2A and E). They are interpreted as contouritic channels based on distinctive reflection continuity from the thalweg of the channel towards a lateral mounded drift basinward, and because their aggradational character resembles the contouritic channels (or moats) as described by different authors (e.g., Fauguères et al., 1999; Garcia et al., 2009; Rebesco et al., 2014). The geometry of these channels is unlike that of Channel System I as recorded in subunit Q4 which are wider, more incised, and exhibit fewer lateral migration structures (Fig. 2B and 2C). Channel System I can be interpreted as the precursor of the present-day Huelva contourite channel. Its channel stacking pattern may record several periods of enhanced or diminished MOW and the influence of diapiric ridges migration.

5.2. Medium-scale interpretation: sandier deposits over the drift

The serrated gamma-ray trend that appear in the upper part of subunit Q4 suggests alternations of sandier inputs interbedded within the finest sediment at Site U1389 (Fig. 3). In other geological settings the serrated gamma-ray trend marks aggrading flood plain deposits in fluvial systems (Cant et al., 1992) or channel-levee turbiditic systems (Hubbard et al., 2009) whose sandy deposits represent overbank events. Because the upper part of Q4 Channel System I and Channel System II were coeval in time, the serrated gamma-ray trend may represent interbedded sandy deposits within the drift due to sediment supply from the adjacent Channel System I levee. The drift became more influenced upwards (especially after the MPD) by the lateral migration of the Channel System II.

The coarsening-upward, funnel-shaped gamma-ray trend seen for subunit Q5 (Fig. 3) suggests an increased sandy input into the drift during a period of enhanced MOW, when the adjacent contouritic channel became more active (Fig. 3). A coarsening-upward trend is usually interpreted as a prograding siliciclastic succession in fluvial and shallow-marine systems. Although its interpretation can be extended to deep-water deposits (Rider and Kennedy, 2011), the classical siliciclastic succession view does not necessarily apply to contourite channel dynamics.

Contourite channel activity depends on the strength of water mass cores migrating laterally due to the Coriolis effect (Faugères et al., 1999; Llave et al., 2001). Their sediment

often comes from gravity-driven flows, reworked along the contourite channels (Hernández-Molina et al., 2006, 2016; Stow et al., 2013). Therefore, an increasing number of sandy beds within the adjacent drift during deposition of subunit Q5 can be attributed to a greater sediment supply from the slope plus an enhanced MOW. In this scenario, sandy sediment could intermittently overspill the drift. We propose that in a contourite system, sandy deposits identified along the drift may be interpreted as the coarser-grained overbank inputs from the adjacent contouritic channel (or moat). The sandier sediments are interstratified with finer-grained (muddy) drift deposits. The fact that the top of subunit Q5 has linear gamma-ray trend packages might reflect the combined effects of active periods of Channel System II migration/avulsion and periods of channel inactivity (Fig. 3).

5.3. Small-scale interpretation: sedimentary facies

Facies 1 (F1)

The structureless, fine silts may represent hemipelagic deposits or very fine-grained (<15 μm) contourites influenced by very weak (<5-10 cm sec^{-1}) bottom currents with suspension load (Brackenridge et al., 2018). This facies exhibits normal platykurtic to mesokurtic grain size distributions (Figs. 4, 5 and 10), which are typical of hemipelagic deposits (Brackenridge et al., 2018). The low $\ln \text{Zr/Al}$ indicates that this facies was emplaced with a very weak or no bottom current. The high $\ln \text{Ca/Sr}$ reflects a dominant planktic foraminifers and nannofossil contribution above shallow-marine bioclasts (Fig. 12), indicating settled particles. In addition, the dominant microstructures detected by SEM suggest that F1 was also either deposited under weak bottom current conditions (Fig. 8A) (Nishida, 2016) or represents the deposition from flocculated suspension fallout during waning phases of very low-density gravity flow (Kase et al., 2016) (Fig. 8B). Yet, if they are part of a diluted turbiditic flow, such deposits can be considered hemiturbidites (Stow and Wetzel, 1990).

Sedimentological and ichnofacies characteristics thus indicate that F1 may be the result of deposition by suspension fallout in conjunction with the lateral advection of fine-grained terrigenous particles (Hesse, 1975; O'Brien et al., 2009) periodically affected by bottom currents. This facies represents the regional background sedimentation along the middle slope; it may signal complete gradation of hemipelagites, hemiturbidites and muddy contourites, as bottom-current velocity increases. Due to the internal complexity of F1, further work is needed to evaluate in detail its nature and variability.

Facies 2 (F2)

The massively- to normally-graded sharp-based beds suggest an abrupt change in depositional conditions with respect to F1, as well as erosion at the base of F2, which supports the interpretation of rapid sediment input into the system by a sediment gravity flow. The presence or absence of traces in F1 infilled by coarser material (F2) observed here may reflect the rate and continuity of sedimentation from F1 to F2, as proposed Rodríguez-Tovar et al. (2015a, b). A rapid, voluminous, and continuous deposition of F2 would inhibit bioturbation by tracemakers in F2 and, by extension, tracemaker penetration from F2 into underlying F1 (Fig. 6G). Although small-scale scour/erosive surfaces suggest a turbulent state of the flow in some cases, this does not mean that the coarse-grained silt in F2 resting on the scour surface was deposited by the same turbulent flow that created the scour surface (Sanders, 1965). Peakall et al. (2020) recently demonstrated that the erosive surface and overlying deposits can be produced by different types of current. The erosive surface could therefore have no genetic link to the overlying turbidity current deposit, and a substantial time gap between erosion and deposition may be considered. This is in agreement with discontinuous deposition between F1 and F2, which would favour bioturbation before F2 deposition and could explain the passively infilled *Thalassinoides* traces and traces infilled by F2 sediment found in F1 (Fig. 6A-E). In addition, the presence of *Planolites* traces toward the top of F2 would indicate an interruption in sedimentation after F2 (Rodríguez-Tovar et al. 2019b). The sharp basal contact and massive to normal gradation support that F2 formed from low-density turbidity currents as suggested by previous authors (Lowe, 1982; Postma, 1986; Stanley 1987, 1988, 1993).

Facies 3 (F3)

A sharp basal contact in F3 indicates erosion and/or reworking from previous turbiditic deposits (F2). This sharp surface was likely formed by tractive processes that progressively eroded and reworked a graded sand turbidite layer (Stanley, 1987, 1988, 1993). Above this contact, a decrease in the fine-grained fraction, an inverse grading trend, and the presence of subhorizontal, mud-rich, and mud-free laminations indicate short periods of enhanced hydrodynamic conditions during F3 deposition (Fig. 4). Most fossil sandy contourites show subhorizontal, heterolithic lamination; this would indicate deposition under the influence of weak to moderate, fluctuating bottom currents, and alternations of suspension and traction processes (Shanmugam, 2000; Ito, 2002; Capella et al., 2017; Hüneke et al., 2020). In F3 it is common to find intraclasts that share composition and texture with F1 (Fig. 7A and 7C). Intraclasts moreover attest to the presence of hardened sediments near the sediment interface

(Gambacorta et al., 2014), possibly eroded by bottom current activity. Altogether, the sharp boundary with F2, the presence of intraclasts and the winnowing of the finest fraction allow us to interpret F3 as sediment reworked by bottom currents after turbiditic deposition when thin-laminated tractive sedimentary structures began to develop (see section 5.4 for further discussion).

Facies 4 (F4)

Lenticular bedding with matrix-free and well-sorted, very fine sand in F4 is interpreted as ripples. Sedimentological characteristics in F4 include evidence of sedimentary condensation, interruption of sedimentation, reactivation and condensation surfaces, and intermittent changes in flow velocity. Grain size distribution curves show a lesser fine-grained fraction for all samples analysed when compared to the other facies (Fig. 4). The concentration of opaques within matrix-supported laminae is taken to represent iron exchange and mineralogical evolution at the sediment/water interface (Giresse, 2009). Fine-grained laminae suggest low sedimentation rates and condensation of oxides in the sediment. The identified ichnological record provides further evidence of interrupted sedimentation during F4 deposition (Rodríguez-Tovar et al. 2019a). Though scarce, some trace fossils appear as isolated burrows (Fig. 6B and 6C) or as burrows localised in given horizons (Fig. 6A and 6E). The presence of discrete burrows, mainly *Planolites*, in specific horizons supports interpretation of discontinuous deposition with intervals of condensation that allowed simultaneous bioturbation by *Planolites* (shallow tier structures) at or slightly below the seafloor (Rodríguez-Tovar and Uchman, 2004, 2006; Rodríguez-Tovar and Dorador, 2014; Łaska et al., 2017; Rodríguez-Tovar et al., 2019a, b). Traces were produced during phases of favourable conditions when lower sedimentation rates allowed for bioturbation.

The heterolithic texture of F4, which includes matrix- and grain-supported alternations, suggests changes in flow velocity; enhanced upward velocity is indicated by inverse grading and the truncation of rippled laminae at the top of F4 (Fig. 6). Therefore, F4 is believed to have formed by means of vigorous but intermittent bottom currents strengthening upwards and developing ripples of well-sorted sands. This interpretation is in line with the proposal of other authors: Shanmugam et al. (1993) and Shanmugam (2000) proposed lenticular bedding and sediment starved ripples at core scales as diagnostic criteria for bottom current reworked sands (BCRS). Stanley (1988) and Ito (2002) recognised similar features in upper surfaces of reworked turbidites, while Martín-Chivelet et al. (2008) suggested that prolonged bottom current activity at the sea floor generates rippled intervals.

Facies 5 (F5)

The general lack of primary sedimentary structures, very poorly-sorted sediment, and a relatively high level of mixing produced by extensive bioturbation complicate the interpretation of F5. The basal contact of F5 is transitional from F4, possibly indicating very dilute suspension clouds. Several horizons with traces suggest discontinuous sedimentation favouring discrete phases of bioturbation. The *Planolites/Thalassinoides* alternance as isolated burrows indicates increasing substrate cohesion from softground to hardground conditions. *Planolites* bioturbation horizons and the presence of *Thalassinoides* mark a break in sedimentation that has led to early compaction (hardground) after initial softground (Rodríguez-Tovar et al., 2019a). A lower rate of sedimentation would support the continuous, sparsely distributed bioturbation. This suggests that the energy regime during F5 formation is also episodic. Therefore, F5 is thought to represent a combination of a number of distal turbidity currents slightly reworked by intermittent bottom currents, the bounding surfaces becoming amalgamated or lost due to intense bioturbation and occasionally beds preserve original characteristics (Fig. 8D). The progressive transition from F5 to F1 in the sedimentary sequence (Fig. 6) shows that the environment returned to background sedimentation along the slope at the base of the sequence (F1). This facies transition resembles the upper part (C4 and C5 intervals) of classic bi-gradational carbonate sequences (Gonthier et al., 1984; Faugères et al., 1984; Stow and Faugères, 2008; Blackenridge, 2013; Rebesco et al., 2014), containing similar ichnofacies (Rodríguez-Tovar et al. 2019b).

6. Discussion

6.1. Facies association: evidence of reworking and sedimentary condensation

A common issue in interpreting deep-water sands is the occurrence of parallel laminae and current ripple laminae, usually interpreted in a Bouma Sequence as Tb-Tc divisions (Fig. 13A) in view of the hydraulic fractionation of the flow components (Bouma, 1962). The settled sediment sequence preserves typical grading. It is a typical model of a traction/suspension fallout process. However, if the process is stopped (or seriously affected) from further movement and transport as bedload, it develops reworked depositional features that will be analogous to the plane-parallel (Tb) and current rippled laminae (Tc) as reported by Stanley (1988) and Shanmugam (1997). In this study, the identified sedimentary sequence F1, F2, F3, F4, F5 and F1 (Fig. 13B) records: background sedimentation (F1) later influenced by the initial deposition of a gravity-driven flow (F2), followed by a period of bottom current

reworking (F3 and F4). F3 and F4 interpretation is compatible with the bottom current reworked sands (BCRS) and mixed facies associations (Stanley, 1988; Shanmugam et al., 1993; Shanmugam, 2000; Ito, 2002; Mutti et al., 2012, 2014; Gong et al., 2016) in which lateral and vertical facies associations result from a combination of gravity-driven flows and bottom current processes.

Long-term gravity currents usually induced by river-generated underflows (so-called hyperpycnal flows) can also provoke similar sedimentary sequences. Hyperpycnal flows are strictly viewed as the product of plunging plumes loaded with fine-grained sediment transported by the flow as suspended load (Mutti, 2019). The hyperpycnite sequence (Mulder et al., 2001, 2002) consists of a bi-gradational sequence —a basal coarsening-upward unit capped with a fining-upward unit, and commonly containing continental flora (Mulder et al., 2013). Sedimentary structures and a clear sorting suggest that the flows are usually low-concentrated, and that particle settling and traction acts simultaneously. The most common structures are climbing ripples (Migeon et al., 2001; Mulder et al., 2002, 2003; Mutti et al., 2002), and their presence supports the occurrence of sedimentation continuously, with a suspended particle load that is sometimes larger than particle transport. These particular features do not correspond to the sequence described here. The studied sites are located in a contouritic terrace in the middle slope affected by at least two different vigorous water masses, the Eastern North Atlantic Central Water (ENACW) and the Mediterranean Outflow Water (MOW). Site U1389 is bounded by two contourite channels (Huelva and Guadalquivir), while Site U1388, in the Northern contourite channel, totally disconnected from the shelf. As any flow coming directly from shelf or river discharge would have to move down crossing these well-stratified water masses. These flows would propagate in these water masses and eventually die out after losing their load.

The identified sedimentary sequence does not resemble classic turbiditic sequences (Bouma, 1962; Lowe, 1982) (Fig. 13A) given the evidences of bottom current action in F3 and F4, which includes: a) winnowing in heterolithic beds; b) concentration of oxides and heavy minerals; c) quartz accumulation; and d) trace fossil distribution and infill.

a) A winnowing effect is suggested by the cleaning-upward trend observed from F2 to F4. The size of quartz grains remains relatively constant from F2 to F4, but their texture shifts from matrix-supported to grain-supported (Fig. 7). Accordingly, the BCRS sequence does not represent a single event but rather reworking by progressively more vigorous currents. These result in better sorting and, in some cases, upward coarsening in the sequence (Fig. 5). The heterolithic sedimentary texture in deep-marine environments includes lens-like,

starved ripples; indeed, they serve as diagnostic criteria for reworking by intermittent bottom currents and can be considered as a sedimentary condensation. Sedimentary condensation results from a hydrodynamically active sedimentary regime, which is capable to winnow, erode, rework sediments, and let sediments pass by, and through which authigenic processes are catalysed (Föllmi, 2016). Alternating high- and low-energy conditions are accompanied by bedload deposition and suspension fallout (Stanley, 1988; Shanmugam, 2000; Ito, 2002; Capella et al., 2017; Hüneke et al., 2020). Shanmugam (2008) proposed that deep-marine tidal bottom currents generate such alternation. In turn, Rodríguez-Tovar et al. (2019b) and Hüneke et al. (2020) suggested that fluctuating bottom currents characterise deposition for all contourite divisions (especially the C3 division in the standard contourite bi-gradational sequence; Fig. 13C). The development of matrix-free and matrix-rich alternations would thus be a consistent indicator of bottom current activity.

- b) The concentration of oxides and heavy minerals in F3 and F4 (indicated by high Zr/Al ratios) further indicates bottom current winnowing and removal of fine-grained sediment (Fig. 9). The reworking of sandier sediments produces higher concentrations of heavy minerals during periods of low sedimentation rates and condensation (Stanley, 1988; Giresse and Wiewióra, 2001; Gonthier et al., 2003; Giresse, 2008). Coupled with stable flow strength within a narrow velocity range (20 to 30 cm/s for very fine sands based on Stow et al., 2008), these conditions generated the ripples identified in F4. A similar facies has been described from Upper Cretaceous rocks in St. Croix, U.S. Virgin Islands (Stanley, 1987, 1988), the Niesenflysch in Switzerland, the Annot Sandstone in the French Maritime Alps (Stanley, 1993), Pliocene and Pleistocene Ewing Bank Oilfield deposits in the Gulf of Mexico (Shanmugam et al., 1993), and Paleogene sandstones of the Campos Basin of Brazil (Mutti et al., 2012, 2014). While these conditions rarely occur in most sedimentary environments—including turbidity currents—they do exist in environments influenced by thermohaline currents (Martín-Chivelet et al., 2008).
- c) Quartz accumulation in F3 and F4 shows exhibited distinctive geochemical features. The Si/Ti cross-plots (Fig. 12B) depict a linear relationship among facies that does not include F3 and F4. The relative enrichment in Si versus Ti may result from the lower matrix content and relative enrichment in quartz grains, since clay minerals preferentially adsorb Ti (Fig. 12F). The decrease of $\ln Ca/Ti$ with increasing $\ln Zr/Al$ and the lack of correlation between $\ln Ca/Sr$ and $\ln Si/Al$ in F3 and F4 (Fig. 12E and 12F) indicate winnowing of the finer-grained, carbonate fraction and concentration of coarser quartz grains by enhanced currents (Tallobre et al., 2019). At SEM scale, a mix of well-rounded, sub-angular quartz

grains in F4 (Fig. 8C) suggests different sources for the quartz grains and associated sediment.

- d) Sediment reworking during condensation is mainly a physical process, but biological processes such as bioturbation assist also (Föllmi, 2016). Trace fossil distribution and infill in F3 and F4 occur preferentially in horizons that record periods with lower sedimentation rates or interrupted sedimentation (i.e., Ekdale et al., 1984; Rodríguez-Tovar et al. 2019a, b).

Although some features listed above could be attributed to either turbiditic origin or bottom-current reworking, the association of the several of them improves chances of distinguishing reworked turbidites from other depositional facies.

6.2. Depositional model

By integrating observations made at large, medium and small scales we arrived at the depositional model summarised in the Figure 14. Local structural highs, marginal valleys and diapiric ridges developed since the early Pleistocene controlled slope basin evolution and formation of the main discontinuities (EQD, MPD, and LQD). These features also influenced the distribution and activity of turbiditic (Channel System I) and contouritic channels (Channel System II) (Fig. 2B). Towards the end of subunit Q4 deposition and during deposition of subunit Q5, these channels were active, and the Huelva mounded drift (Fig. 2D; Llave et al., 2007) formed parallel to the adjacent contouritic channel (Channel System II; Fig. 14A). The development of this erosive system is associated with circulation of the upper MOW core and constrained by the diapiric ridges and the Guadalquivir Bank. Together, these processes generated the Huelva contouritic channel (Hernández-Molina et al., 2006; Llave et al., 2007; Brackenridge et al., 2013; Sánchez-Leal et al., 2017). Present day bottom currents resulting from MOW reach velocities of >0.6 m/s when they flow through these bathymetric features and contouritic channels. This figure contrasts with the much lower (0.1 m s⁻¹) velocities of the MOW along the drift (Sánchez-Leal et al., 2017).

In addition to marginal valleys, down- and along-slope channels (Channel Systems I and II, respectively) are evident at seismic scales. They record the interaction processes affecting the middle slope during the middle Pleistocene (Fig. 14A). Marginal valleys were simultaneously active along the NW flanks of diapiric ridges (Fig. 14A) and favoured down-slope circulation (García et al., 2009). Similar processes took place on the mounded drift near the contourite channel, according to the BCRS sequences at Site U1389 (Fig. 14A), where interactions between down- and along-slope processes are recorded as well (Fig. 14A).

F1 evidences a continuum of background deposition from hemipelagic settling, under the influence of dilute, low-density turbidity currents and weak bottom currents —a quiet environment within the drift (1 in Fig. 14B). These deposits show coarser-infilled *Thalassinoides* or lack trace fossils entirely (respectively 2a and 2b respectively in Fig. 14C). In turn, F2 shows turbiditic deposition influenced by interactions between vigorous bottom currents and down-slope circulation. Turbidity currents erode the seafloor on this part of the drift and favour the passive, coarser infilling of bioturbated features found in F1 (3 in Fig. 14C). The presence of *Planolites* horizons at the top of F2 suggests that its deposition was followed by a gap between F2 and F3 (4a in Fig. 14C) as it was proposed by Rodríguez-Tovar et al. (2019a). The absence of trace fossils in F2 also points to rapid sedimentation by flows (4b in Fig. 14C).

Meanwhile, the transitional or sharp contact between F2 and F3 suggests coeval or diachronous interactions between the suspension cloud and bottom currents. Recent flume experiments help clarify ripple development on mixed clay-sand substrates through the effects of clay winnowing (Wu et al., 2018). Hydrodynamic forces are known to suspend fine particles from beds with a bimodal or multimodal grain size distribution, as F2 in this sequence, leaving behind relatively coarse particles (F3 and F4) (e.g., Kleinhans, 2004; Liang et al., 2007). This sorting process makes current ripples in mixed clay-sand become increasingly sandy upwards (Baas et al., 2013; Malarkey et al., 2015): the more clay content, the longer it takes for the first ripples to form. F2 presents more concentration of clay-silt than F3 or F4 (Fig. 4 and 5) meaning some time transpired since the initial evidence of bedforms in the seafloor (5 in Fig. 14C).

We suggest that during this period, *Planolites* had enough time to disturb the substrate (4a and 5 in Fig. 14C and 15A). Shear stress was transmitted by F2, at an early stage of deformation, while F3 developed (6 in Fig. 14D). Under these conditions, even the largest and the least mobile particles could be transported down-current (Fig. 15B). During the maximum shear stress stage, the top of the buried, cohesive F1, would have been exposed and disrupted; thus, erosion began to deliver F1 intraclasts during F3 deposition (Fig. 7A, C and 15B). Cohesive effects were less relevant for particles coarser than 62 μm , hence the decrease in critical bed-shear stress for increasing particle size (Baas et al., 2013) as observed gradually from F2 to F4. The F4 ripples became sandier owing to the effects of reworking, winnowing and bedform migration, and a continuous cover of mobile sand started to protect the underlying mixed sand–mud intervals (F2 and F3; 7 in Fig. 14D). Reworking and winnowing facilitated the formation of migrating clean-sand ripples (Wu et al., 2018). This

enrichment of the bed surface of larger sand grains, together with cohesive bed strength of underlying deposits as F2, may have reduced the winnowing of clay from F2-F3, thus limiting the supply of sand needed for bedform development; essentially forming sediment-starved bedforms (Allen, 1968). Down-current of the winnowing, the coarsest grains (very fine- and fine-grained sand) probably travelled at the base of a winnowing cloud, whereas the light grains (fragmented foraminifera and silt) were incorporated into the suspended cloud (Fig. 15B), which could deposit different beds down-current (Gambacorta et al., 2014). Such changes in energy regime are difficult to attribute to the action of a simple waning flow, and they do not fit classic turbidite interpretations.

After F4 deposition, bottom currents grew weaker but still captured the fine-grained fraction and lateral sediment from dilute turbiditic currents forming F5 (Figs. 14E and 15C). Over time, turbiditic flows became more dilute, with weaker bottom currents and a dominated hemipelagic setting (Fig. 14F). This led to a subsequent F1 above the BCRC sequence. The vertical trend in the BCRC sequence records long-term variations in sediment supply, bottom currents, and turbiditic flow strengths, along with shorter changes variation in turbidite-contourite interactions.

6.3. Bi-gradational sequence vs. BCRC sequence

A bi-gradational sequence (Fig. 13C) on contouritic drifts consisting of five intervals (C1-C5) represents a diagnostic criterion for contouritic deposits (Gonthier et al., 1984; Faugères et al., 1984; Stow and Faugères, 2008). Sedimentary sequences described in the present study include a contourite drift adjacent to a contourite channel (Fig. 14A and 16), which record both turbiditic and contouritic processes (Fig. 15) in progressively reworked sediment.

The F1 to F5 sedimentary sequence (with return to F1) includes coarsening- (from F1 to F4) and fining-upward trends (from F4 to F5+F1) that resemble standard bi-gradational contourite sequences according to Gonthier et al. (1984) and Faugères et al. (1984). Like the intervals later proposed by Stow and Faugères (2008), the sequence described here resembles a “base-cut” bi-gradational contourite sequence: F1 would correspond to the C1 interval, F3 and F4 to C3, F5 to C4, and the uppermost F1 to C5 (Fig. 13C). As shown in Fig. 13B, F2 would thin-out laterally in more distal parts in the drift (respect to the adjacent contourite channel) being substituted by the C2 interval in which bottom currents reworked the previously deposited turbidite event. (Fig. 16). The BCRC would therefore form part of a partial bi-gradational contourite sequence where the initial deposition of gravity-driven flow (F2) is followed by its reworking by bottom currents (F3, F4, and F5).

Stow and Faugères (2008) and Brackenridge et al. (2018) studied incomplete sequences and very well-sorted, massive, medium-grained contourite sand successions identified in other drifts during the drilling IODP Expedition 339 (Expedition 339 Scientists, 2012; Stow et al., 2013b; Hernández-Molina et al., 2013, 2016b). Alonso et al. (2016) describe base-cut contourite sequences from areas near contourite channels and moats. The deposits reported here stand as a novel example of a turbiditic remnant deposit within a contouritic drift that records the classic bi-gradational sequence (Gonthier et al. 1984; Faugères et al., 1984). As such, this deposit sheds light on relations between contourite sequences and turbiditic flows carrying sandy sediment. Turbiditic flows can specifically transport sandy sediments (F2) into a contouritic drift, where they are subjected to bottom current reworking and winnowing (F3, F4, and F5).

The classic bi-gradational sequence (Fig. 13C) lacks primary sedimentary structures in the central sandier interval (C3) due to vigorous bioturbation, as weaker energy conditions prevailing in this relatively distal area on the drift (Gonthier et al. 1984; Stow and Faugères, 2008). By contrast, the sedimentary sequence described here formed in a more proximal lateral location (with respect to the adjacent contourite channel) on the drift (Fig. 16). Bottom currents at this locality remained strong enough to winnow fine-grained sediment and prevent disruption of primary sedimentary structures due to bioturbation. Situated between the contourite channel and drift, this setting differs from others (Fig. 17) that host reworked turbidites and BCRS (Stanley, 1988; Shanmugam et al., 1993; Shanmugam, 2000; Ito, 2002; Mutti et al., 2012, 2014; Gong et al., 2016), and from sand-prone deep-sea fans mixed systems (Sansom, 2018; Fornesù et al., 2020; Fuhrman et al., 2020). The presence and preservation of BCRS (F3 and F4) in the sedimentary sequence thus demonstrates the proximity of down-slope systems with respect to the contouritic drift, and the intermittency, coexistence, and relative energy of down- and along-slope currents.

6.4. Temporal distribution of partial bi-gradational contourite sequences including BCRS

Chronostratigraphic constraints can help researchers to understand partial bi-gradational contourite sequences including BCRS within contourite drifts. According to sequence stratigraphic models proposed for the Gulf of Cadiz (Llave et al., 2001, 2006, 2007; Hernández-Molina et al., 2002, 2016b; Roque et al., 2012), dominant down-slope gravity flows occurred primarily during relative sea-level fall and lowstand stages. During these episodes, shorelines moved closer to the shelf edge and the upper MOW activity weakened (or eventually disappeared) (Mestdagh et al., 2019). In colder glacial stages, a denser and

more intense MOW (relative to present) caused enhanced lower MOW flow (Schönfeld and Zahn, 2000; Schönfeld et al., 2003; Llave et al., 2006; Voelker et al., 2006; Rogerson et al., 2012; Bahr et al., 2014). Lower sea-level during glacial stages therefore leads to both abundant turbiditic flows and enhanced bottom currents along the middle slope.

Given these factors, the proposed, partial bi-gradational contourite sequences that include BCRS could be tentatively interpreted as influenced by climatic and sea-level oscillations during glacial-interglacial stages or stadial-interstadial periods. Down-slope sediment gravity flows predominate as slope processes during colder periods (relative lowstands). Once they reach the drift (F2) in space, they are reworked by vigorous along-slope bottom currents (F3 and F4). During transitions (colder to warmer or warmer to colder, and respective transgressions/regressions) dilute turbiditic flows occur along down-slope areas due to sea-level rise coeval with weaker bottom currents (F5). In warm periods (relative highstands), middle slope areas are dominated by hemipelagic settling with fine-grained turbidity currents and fine-grained contourites (F1). The alternation between hemipelagic, turbidity currents and contouritic sedimentation and its link with sea-level changes, evoke the sedimentary evolution model proposed for the Pianosa COS in the Tyrrhenian Sea (Miramontes et al., 2016). Yet, interpretations linking sequences to climatic factors must consider that the proposed age for the bi-gradational contouritic sequences varies from 3 to 10 ky (Llave et al., 2006; Brackenridge et al., 2018). Therefore, these intervals do not match stadial and interstadial cycles, affected by higher resolution variation at millennial scales. In addition, the best studied partial bi-gradational contourite sequences that include BCRS also occur during a specific Pleistocene interval, at two different localities hosting the same contourite system — the proximal (Site U1388) and central (Site U1389) sectors of the Gulf of Cadiz. Further research is needed to constrain the timing of when these sequences formed.

6.5. Implications for petroleum exploration

Large amounts of well-sorted sands can be found in the channels and terraces of contouritic depositional systems (Viana, 2008; Mutti et al., 2012; Stow et al., 2013a; Hernández-Molina et al., 2016a; Brackenridge et al., 2018). These deposits offer good reservoir properties. In adjacent contourite drifts, the drift mud-to-sand ratio increases, so that large muddy drifts can act as seals (Viana, 2007, 2008).

The partial bi-gradational contourite sequences including BCRS (F3 and F4) host sandy horizons that extend laterally from the contourite channels and over the drift. These probably occur as patchy lenticular bodies and do not form extensive sand sheets as proposed by

previous authors for other BCRS systems (Ericson et al., 1961; Shepard and Einsele, 1962; Stanley, 1987, 1988, 1993; Shanmugam et al., 1993). This sand distribution may imply to lateral changes in the seafloor and redistribution of sand in a sediment-starved system (Stanley, 1988). Partial bi-gradational contourite sequences including BCRS are not continuous within a contourite drift, they do show relatively heterogeneous porosity on the scale of the entire deposit. Within a predominately fine-grained drift, BCRS (F3 and F4) could have either poor or good reservoir potential in terms of porosity and volume.

6. Conclusions

The sedimentological characteristics of BCRS proposed here contribute to establishing a set of diagnostic criteria to recognise of bottom-current reworking. However, it is important to be aware that no single sedimentological described herein is unique to BCRS. Some features listed in this work can signal either turbiditic origin or bottom-current reworking; it is the association of all of them, at different scales, that helps distinguish BCRS.

This work defines partial bi-gradational contourite sequences containing BCRS formed by the interaction of down- and along-slope processes within contourite drifts adjacent to contouritic channels and marginal valleys. FCRS are typified by heterolithic, matrix-free, and matrix-rich ripple-laminated aggradational deposits made up of very-fine sands. BCRS can reach 30 cm in thickness and may be interbedded with up to 12 m of fine silt. The sequence is moderately bioturbated and contains distinctive trace fossil assemblages, often dominated by ichnofabrics of the *Planolites* and *Thalassinoides*. These assemblages represent intermittent deposition between down- and along-slope processes during relatively short time scales. Previous models for BCRS described their formation as linked to submarine canyons or distal submarine fans under the influence of relatively weak bottom currents. This work presents a novel sedimentary model for contouritic drifts influenced by turbiditic flows.

In this model, down- and along-slope sediment transport processes interact with vigorous bottom currents to rework deposits initially formed by low-density turbidity currents. Erosion, reworking, sedimentary condensation, and interruption of sedimentation generate the diagnostic evidence for sedimentary sequences that include BCRS. Our data show that along-slope reworking is intermittent at short time scales. They generate marked alternations in matrix-rich and matrix-free heterolithic textures. Long-term trends, however, reflect increases and decreases in both sediment supply and bottom current velocity.

Contourites and BCRS are common types of deep-water sedimentary deposits along continental margin settings. They may be seen as critical depositional settings for research

addressing present and ancient marine records. Future research is needed to clarify the diversity of lateral and vertical associations, pelagic/hemipelagic and turbiditic flows, bottom currents and mass transport processes and how these deposits record continental margin stacking patterns.

Acknowledgments

This project was funded through the Joint Industry Project supported by BP, ENI, TOTAL, ExxonMobil, Wintershall Dea and TGS, within the framework of “The Drifters” Research Group at Royal Holloway University of London (RHUL), and is related to the projects CTM 2012-39599-C03, CGL2015-66835-P, CTM2016-75129-C3-1-R and B-RNM-072-UGR18. Additional funding was provided in the form of postgraduate research and travel grants by the IAS. This research used data and samples collected through IODP Expedition 339 aboard the Joides Resolution. Data was acquired at the XRF Core Scanner Lab at the MARUM – Center for Marine Environmental Sciences, University of Bremen, Germany. Our thanks to Dr. Javier Dorador (RHUL, UK) for the high-resolution core imaging treatment, Dr. Andrea Ortenzi (ENI) for help in identifying evidence of reworking using the SEM at Bolgiano laboratories (ENI SpA, Milan, Italy), Dr. Domenico Chiarella (RHUL, UK) and Dr. Ángel Puga-Ernabéu (University of Granada, Spain) for its discussion and revision that helped us to improve the original version of the manuscript before submission. We also thank Dr. Eida Miramontes, Dr. Marco Fomesu and a third anonymous reviewer for their constructive comments.

Declaration of Interest statement

We declare that we do not have any commercial or associative interest that represents a conflict of interest in connection with the work submitted.

References

- Alonso, B., Ercilla, G., Casas, D., Stow, D.A., Rodríguez-Tovar, F.J., Dorador, J. Hernández-Molina, F.J. 2016. Contourite vs gravity-flow deposits of the Pleistocene Faro Drift (Gulf of Cadiz): Sedimentological and mineralogical approaches. *Mar. Geol.*, 377, 77-94.
- Allen, J. L. 1968. Current ripples.

- Ambar, I. and Howe, M.R. 1979. Observations of the Mediterranean outflow—I mixing in the Mediterranean outflow. *Deep Sea Research Part A. Oceanographic Research Papers*, 26(5), 535-554.
- Azpiroz-Zabala, M., Cartigny, M.J., Talling, P.J., Parsons, D.R., Sumner, E.J., Clare, M.A., Simmons, S.M., Cooper, C., and Pope, E.L. 2017. Newly recognized turbidity current structure can explain prolonged flushing of submarine canyons. *Science advances*, 3(10), e1700200.
- Baas, J. H., Davies, A. G., Malarkey, J. 2013. Bedform development in mixed sand–mud: The contrasting role of cohesive forces in flow and bed. *Geomorphology*, 182, 19-32.
- Bahr, A., Jiménez- Espejo, F.J., Kolasinac, N., Grunert, P., Hernández- Molina, F.J., Röhl, U., Voelker, A.H., Escutia, C., Stow, D.A., Hodell, D., Alarez- Zarikian, C.A. 2014. Deciphering bottom current velocity and paleoclimate signals from contourite deposits in the Gulf of Cádiz during the last 140 kyr: An inorganic geochemical approach. *Geochemistry, Geophysics, Geosystems*, 15(8), 3145–3160.
- Bahr, A., Kaboth, S., Jiménez-Espejo, F.J., Sierco, F.J., Voelker, A.H.L., Lourens, L., Röhl, U., Reichart, G.J., Escutia, C., Hernández-Molina, F.J., Pross, J. 2015. Persistent monsoonal forcing of Mediterranean Outflow Water dynamics during the late Pleistocene. *Geology*, 43(11), 951-954.
- Baringer, M.O.N. and Price, J.F. 1999. A review of the physical oceanography of the Mediterranean outflow. *Mar. Geol.*, 155(1-2), 63-82.
- Blott, S.J. and Pye, K. 2001. GRADISTAT: a grain size distribution and statistics package for the analysis of unconsolidated sediments. *Earth Surf. Proc. Land.*, 26(11), 237-248.
- Baccelle, L. and Bose lini, A. 1965. Diagrammi per la stima visiva della composizione percentuale nelle rocce sedimentarie. Università degli studi di Ferrara. Vol 4, No 3.
- Bouma, A. H. 1962. Sedimentology of some flysch deposits. A graphic approach to facies interpretation, 168.
- Brackenridge, R.E., Hernández-Molina, F.J., Stow, D.A.V. Llave, E. 2013. A Pliocene mixed contourite–turbidite system offshore the Algarve Margin, Gulf of Cadiz: seismic response, margin evolution and reservoir implications. *Mar. Petrol. Geol.*, 46, 36-50.
- Brackenridge, R. E., Stow, D. A., Hernández- Molina, F. J., Jones, C., Mena, A., Alejo, I., Ducassou, E., Llave, E., Ercilla, G., Nombela, M.A., Pérez- Arlucea, M., Frances, G. 2018. Textural characteristics and facies of sand- rich contourite depositional systems. *Sedimentology*, 65(7), 2223-2252.

- Bryden, H.L. and Stommel, H.M. 1982. Origin of the Mediterranean outflow. *J. Mar. Res.*, 40, 55-71.
- Bryden, H.L., Candela, J. Kinder, T.H. 1994. Exchange through the Strait of Gibraltar. *Prog. Oceanogr.*, 33(3), 201-248.
- Buitrago, J., García, C., Cajebread-Brow, J., Jiménez, A. and Martínez del Olmo, W. 2001. September. Contouritas: un excelente almacén casi desconocido (Golfo de Cádiz, SO de España). In 1er Congreso Técnico Exploración y producción REPSOL-YPF, Madrid, 24-27.
- Cant, D.J. 1992. Subsurface facies analysis. In: *Facies models, response to sea-level change*, eds. Walker, R.G., James, N.P., Geol. Soc. Canada, 27-45.
- Capella, W., Hernández-Molina, F.J., Flecker, R., Hilgen, F. J., Hssain, M., Kouwenhoven, van Oorschot, M., Sierro, F.J., Stow, D.A.V., Trabucio-Alexandre, J., Tulbure, M.A., de Weger, W., Yousfi, M.Z., Krijgsman, W. 2017. Sandy contourite drift in the late Miocene Rifian Corridor (Morocco): Reconstruction of depositional environments in a foreland-basin seaway. *Sed. Geol.*, 355, 31-57
- Catuneanu, O., Abreu, V., Bhattacharya, J.P., Blum, M.D., Dalrymple, R.W., Eriksson, P.G., Fielding, C.R., Fisher, W.L., Galloway, W.E., Gibling, M.R. Giles, K.A. 2009. Towards the standardization of sequence stratigraphy. *Earth Sci. Rev.*, 92(1-2), 1-33.
- Creaser, A., Hernández-Molina, F.J., Badalini, G., Thompson, P., Walker, R., Soto, M. Conti, B. 2017. A Late Cretaceous mixed (turbidite-contourite) system along the Uruguayan Margin: Sedimentary and paleoceanographic implications. *Mar. Geol.*, 390, 234-253.
- Dasgupta, P. 2003. Sediment gravity flow—the conceptual problems. *Earth Sci. Rev.*, 62(3-4), 265-281.
- Dorador, J. and Rodríguez-Tovar, F.J. 2018. High-resolution image treatment in ichnological core analysis: initial steps, advances and prospects. *Earth Sci. Rev.*, 177, 226-237.
- Dorador, J., Rodríguez-Tovar, F.J., IODP Expedition 339 Scientists. 2014a. Digital image treatment applied to ichnological analysis of marine core sediments. *Facies*, 60, 39-44.
- Dorador, J., Rodríguez-Tovar, F.J., IODP Expedition 339 Scientists. 2014b. Quantitative estimation of bioturbation based on digital image analysis. *Mar. Geol.*, 349, 55-60.
- Dorador, J., Rodríguez-Tovar, F.J., Mena, A., Francés, G. 2019. Lateral variability of ichnological content in muddy contourites: Weak bottom currents affecting organism's behaviour. *Scientific reports*, 9(1), 1-7.

- Duarte, J.C., Rosas, F.M., Terrinha, P., Schellart, W.P., Boutelier, D., Gutscher, M.A., Ribeiro, A. 2013. Are subduction zones invading the Atlantic? Evidence from the southwest Iberia margin. *Geology*, 41(8), 839-842.
- Ekdale, A.A., Bromley, R.G., Pemberton, S.G. 1984. Ichnology: The Use of Trace Fossils in Sedimentology and Stratigraphy. *SEPM Short Course Notes*, 15, pp. 1-316.
- Ercilla, G., Casas, D., Estrada, F., Vázquez, J.T., Iglesias, J., García, M., Gómez, M., Acosta, J., Gallart, J., Maestro-González, A., Team, M. 2008. Morphosedimentary features and recent depositional architectural model of the Cantabrian continental margin. *Mar. Geol.*, 247(1-2), 61-83.
- Expedition 339 Scientists. 2012. Site U1389 Summary. IODP Expedition 339: Mediterranean Outflow. Site Summaries. International Ocean Discovery Program.
- Faugères, J.C., Stow, D.A., Imbert, P., Viana, A. 1999. Seismic features diagnostic of contourite drifts. *Mar. Geol.*, 162(1), 1-38.
- Faugères, J.C. and Stow, D.A.V. 2008. Contourite drifts: nature, evolution and controls. *Developments in sedimentology*, 60, 257-288.
- Folk, R.L. and Robles, R. 1964. Carbonate sands of Isla Perez, Alacran reef complex, Yucatan. *J. Geol.*, 72(3), 255-292.
- Folk, R.L. and Ward, W.C. 1957. Brazos River bar [Texas]; a study in the significance of grain size parameters. *J. Sed. Res.*, 27(1), 3-26.
- Föllmi, K. B. 2016. Sedimentary condensation. *Earth-Science Reviews*, 152, 143-180.
- Fonnesu, F. 2013. The Mamba Complex supergiant gas discovery (Mozambique): an example of turbidite fans modified by deep-water tractive bottom currents. In The 12th PESGB/HGS Conference on African E&P. London: PESGB.
- Fonnesu, M., Palermo, L., Galbiati, M., Marchesini, M., Bonamini, E., Bendias, D. 2020. A new world-class deep-water play-type deposited by the syndepositional interaction of turbidity flows and bottom currents: The giant Eocene Coral Field in northern Mozambique. *Mar. Petrol. Geol.*, 111, 179-201.
- Fuhrmann, A., Kane, I.A., Clare, M.A., Ferguson, R.A., Schomacker, E., Bonamini, E., Contreras, F.A. 2020. Hybrid turbidite-drift channel complexes: An integrated multiscale model. *Geology*, 48.
- García, M., Hernández-Molina, F.J., Llave, E., Stow, D.A.V., León, R., Fernández-Puga, M.C., Del Río, V.D. and Somoza, L. 2009. Contourite erosive features caused by the Mediterranean Outflow Water in the Gulf of Cadiz: Quaternary tectonic and oceanographic implications. *Mar. Geol.*, 257(1-4), 24-40.

- Gales, J.A., Larter, R.D., Mitchell, N.C., Dowdeswell, J.A. 2013. Geomorphic signature of Antarctic submarine gullies: implications for continental slope processes. *Mar. Geol.*, 337, 112-124.
- Giresse, P. 2008. Some aspects of diagenesis in contourites. *Developments in Sedimentology*, 60, 203-221.
- Giresse, P. and Wiewióra, A. 2001. Stratigraphic condensed deposition and diagenetic evolution of green clay minerals in deep water sediments on the Ivory Coast–Ghana Ridge. *Mar. Geol.*, 179(1-2), 51-70.
- Gambacorta, G., Bersezio, R., Erba, E. 2014. Sedimentation in the Tethyan pelagic realm during the Cenomanian: Monotonous settling or active redistribution? *Palaeogeography, Palaeoclimatology, Palaeoecology*, 409, 301-319.
- Gong, C., Wang, Y., Zhu, W., Li, W., Xu, Q. 2013. Upper Miocene to Quaternary unidirectionally migrating deep-water channels in the Pearl River mouth Basin, northern South China Sea. *AAPG Bull.*, 97(2), 285-308.
- Gong, C., Wang, Y., Xu, S., Pickering, K.T., Peng, X., Li, W., Yan, Q. 2015. The northeastern South China Sea margin created by the combined action of down-slope and along-slope processes: Processes, products and implications for exploration and paleoceanography. *Mar. Pet. Geol.*, 64, 233-249.
- Gong, C., Wang, Y., Zheng, R., Hernández-Molina, F. J., Li, Y., Stow, D.A.V., Xu, Q., Brackenkridge, R. E. 2016. Middle Miocene reworked turbidites in the Baiyun Sag of the Pearl River Mouth Basin, northern South China Sea margin: processes, genesis, and implications. *Journal of Asian Earth Sciences*, 128, 116-129.
- Gong, C., Peakall, J., Wang, Y., Wells, M. G., Xu, J. 2017. Flow processes and sedimentation in contourite channels on the northwestern South China Sea margin: A joint 3D seismic and oceanographic perspective. *Mar. Geol.*, 393, 176-193.
- Gonthier, E., Faugères, J.C., Viana, A., Figueiredo, A., Anschutz, P. 2003. Upper Quaternary deposits on the Sao Tomé deep-sea channel levee system (South Brazilian Basin): major turbidite versus contourite processes. *Mar. Geol.*, 199(1-2), 159-180.
- Hansen, L.A., Callow, R.H., Kane, I.A., Gamberi, F., Rovere, M., Cronin, B.T., Kneller, B.C. 2015. Genesis and character of thin-bedded turbidites associated with submarine channels. *Mar. Petrol. Geol.*, 67, 852-879.
- Heezen, B.C. and Hollister, C. 1964. Deep-sea current evidence from abyssal sediments. *Mar. Geol.*, 1(2), 141-174.

- Hernández-Molina, F.J., Somoza, L., Vázquez, J.T., Lobo, F., Fernández-Puga, M.C., Llave, E., Díaz-del Río, V. 2002. Quaternary stratigraphic stacking patterns on the continental shelves of the southern Iberian Peninsula: their relationship with global climate and paleoceanographic changes. *Quat. Int.*, 92, 5-23.
- Hernández-Molina, J., Llave, E., Somoza, L., Fernández-Puga, M.C., Maestro, A., León, R., Medialdea, T., Barnolas, A., García, M., Díaz del Río, V., Fernández-Salas, L.M., Vázquez, J.T., Lobo, F.J., Alverinho Dias, J.M., Rodero, J., Gardner, J. 2003. Looking for clues to paleoceanographic imprints: A diagnosis of the gulf of Cadiz contourite depositional systems. *Geology*, 31, 19-22.
- Hernández-Molina, F.J., Llave, E., Stow, D.A.V., García, M., Somoza, L., Vázquez, J.T., Lobo, F.J., Maestro, A., del Río, V.D., León, R., Medialdea, T. 2006. The contourite depositional system of the Gulf of Cadiz: a sedimentary model related to the bottom current activity of the Mediterranean outflow water and its interaction with the continental margin. *Deep-Sea Res. Part II Topical Stud. Oceanogr.*, 53(11-13), 1420-1463.
- Hernández-Molina, F.J., Llave, E., Stow, D.A.V. 2008. Continental slope contourites. In: Rebesco, M., Camerlenghi, A. (Eds.), Contourites. *Developments in sedimentology*, 60, 379-408.
- Hernández-Molina, F.J., Serra, N., Stow, D.A.V., Llave, E., Ercilla, G., Van Rooij, D. 2011. Along-slope oceanographic processes and sedimentary products around the Iberian margin. *Geo-Mar. Lett.*, 31(5-6), 315-341.
- Hernández-Molina, F.J., Stow, D.A.V., Alvarez-Zarikian, C., Expedition IODP 339 Scientists, 2013. IODP expedition 339 in the gulf of Cadiz and off west Iberia: decoding the environmental significance of the Mediterranean outflow water and its global influence. *Sci. Drill.* 10, 1-11.
- Hernández-Molina, F. J., Stow, D. A., Alvarez-Zarikian, C. A., Acton, G., Bahr, A., Balestra, B., Ducassou, E., Flood, R., Flores, J. A., Furota, S., Grunert, P., Hodell, D., Jimenez-Espejo, F., Kim, J. K., Krissek, L., Kuroda, J., Li, B., Llave, E., Lofi, J., Lourens, L., Miller, M., Nanayama, F., Nishida, N., Richter, C., Roque, C., Pereira, H., Sanchez Goñi, M. F., Sierro, F. J., Singh, A. D., Sloss, C., Takashimizu, Y., Tzanova, A., Voelker, A. H. L., Williams, T., Xuan, C. 2014. Onset of Mediterranean outflow into the North Atlantic. *Science*, 344(6189), 1244-1250.
- Hernández-Molina, F.J., Soto, M., Piola, A.R., Tomasini, J., Preu, B., Thompson, P., Badalini, G., Creaser, A., Violante, R.A., Morales, E. Paterlini, M. 2016a. A contourite

- depositional system along the Uruguayan continental margin: sedimentary, oceanographic and paleoceanographic implications. *Mar. Geol.*, 378, 333-349
- Hernández-Molina, F.J., Sierro, F.J., Llave, E., Roque, C., Stow, D.A.V., Williams, T., Lofi, J., Van der Schee, M., Arnáiz, A., Ledesma, S., Rosales, C. 2016b. Evolution of the gulf of Cadiz margin and southwest Portugal contourite depositional system: Tectonic, sedimentary and paleoceanographic implications from IODP expedition 339. *Mar. Geol.*, 377, 7-39.
- Hernández-Molina, F.J., Campbell, S., Badalini, G., Thompson, P., Walker, R., Soto, M., Conti, B., Preu, B., Thieblemont, A., Hyslop, L., Miramontes, E., Morales, E. 2018. Large bedforms on contourite terraces: Sedimentary and conceptual implications. *Geology*, 46 (1), 27-30.
- Hsü, K.J. 1964. Cross-laminations in graded bed sequence. *J. Sed. Res.*, 34(2), 379-388.
- Hubbard, S.M., de Ruig, M.J., Graham, S.A. 2009. Confined channel-levee complex development in an elongate depo-center: deep-water Tertiary strata of the Austrian Molasse basin. *Mar. Pet. Geol.*, 26(1), 85-112.
- Hubert, J.F. 1964. Textural evidence for deposition of many western North Atlantic deep-sea sands by ocean-bottom currents rather than turbidity currents. *J. Geol.*, 72(6), 757-785.
- Hüneke, H. and Stow, D.A.V. 2008. Identification of ancient contourites: problems and palaeoceanographic significance. in Rebescio, M., Camerlenghi, A. (Eds.), *Contourites. Developments in Sedimentology*, 50, 323-344.
- Hüneke, H., Hernandez-Molina, F.J., Rodríguez-Tovar, F.J., Llave, E., Chiarella, D., Mena, A., Stow, D.A.V. 2020. Diagnostic criteria using microfacies for calcareous contourites, turbidites and pelagites in the Eocene-Miocene slope succession, southern Cyprus. *Sedimentology*, In press.
- IGME. 1987. Contribución de la exploración petrolífera al conocimiento de la Geología de España. Instituto Geológico Minero de España, Madrid, 465 pp.
- Ito, M. 2002. Kuroshio current-influenced sandy contourites from the Plio-Pleistocene Kazusa forearc basin, Boso Peninsula, Japan. *Geol. Soc. London, Memoirs*, 22(1), 421-432.
- Kaboth, S., Bahr, A., Reichert, G.J., Jacobs, B., Lourens, L.J. 2016. New insights into upper MOW variability over the last 150 kyr from IODP 339 Site U1386 in the Gulf of Cadiz. *Mar. Geol.*, 377, 136-145.

- Kane, I.A., Catterall, V., McCaffrey, W.D., Martinsen, O.J. 2010. Submarine channel response to intrabasinal tectonics: The influence of lateral tilt. *AAPG Bull.*, 94(2), 189-219.
- Kase, Y., Sato, M., Nishida, N., Ito, M., Mukuti, M.M., Ikehara, K., Takizawa, S. 2016. The use of microstructures for discriminating turbiditic and hemipelagic muds and mudstones. *Sedimentology*, 63, 2066-2086.
- Kenyon, N.H. and Belderson, R.H. 1973. Bed forms of the Mediterranean undercurrent observed with side-scan sonar. *Sed. Geol.*, 9(2), 77-99.
- Keul, N., Langer, G., Thoms, S., de Nooijer, L. J., Reichart, G. J., Bijma, J. 2017. Exploring foraminiferal Sr/Ca as a new carbonate system proxy. *Geochim. Cosmochim. Acta*, 202, 374-386.
- Kleinhaus, M. 2004. Sorting in grain flows at the lee side of dunes. *Earth-Science Reviews*, 65(1-2), 75–102.
- Kneller, B., Buckee, C. 2000. The structure and fluid mechanics of turbidity currents: a review of some recent studies and their geological implications. *Sedimentology*, 47, 62-94
- Kuenen, P.H. 1964. Deep-sea sands and ancient turbidites. In *Developments in sedimentology*. Elsevier. Vol. 3, 3-33.
- Łaska, W., Rodríguez-Tovar, F.J., Uchman, A. 2017. Evaluating macrobenthic response to the Cretaceous-Palaeogene event: a high-resolution ichnological approach at the Agost section (SE Spain). *Cretac. Res.*, 70, 96-110.
- Liang, H., Lamb, M. P., Parsons, J. D. 2007. Formation of a sandy near-bed transport layer from a fine-grained bed under oscillatory flow. *J. Geophys. Res.*, 112, C02008.
- Llave, E., Hernández-Molina, F.J., Somoza, L., Díaz del Río, V., Stow, D.A.V., Maestro, A., Alveirinho Dias, J.M. 2001. Seismic stacking pattern of the Faro-Albufeira contourite system (Gulf of Cadiz): A Quaternary record of paleoceanographic and tectonic influences. *Mar. Geophys. Res.*, 22, 475–496.
- Llave, E., Schönfeld, J., Hernández-Molina, F.J., Mulder, T., Somoza, L., Díaz del Río, V., Sánchez-Almazo, I. 2006. High-resolution stratigraphy of the Mediterranean outflow contourite system in the Gulf of Cadiz during the late Pleistocene: the impact of Heinrich events. *Mar. Geol.*, 227(3-4), 241-262.
- Llave, E., Hernández-Molina, F.J., Somoza, L., Stow, D.A.V., Díaz del Río, V. 2007. Quaternary evolution of the contourite depositional system in the Gulf of Cadiz. *Geol. Soc., London, Sp. Publ.*, 276, 49-79.

- Llave, E., Hernández-Molina, F.J., Ercilla, G., Roque, C., Van Rooij, D., García, M., Juan, C., Mena, A., Brackenridge, R., Jané, G., Stow, D.A.V. 2015. Bottom current processes along the Iberian continental margin. *Boletín Geológico y Minero*, 126(2-3), 219-256.
- Lofi, J., Voelker, A.H.L., Ducassou, E., Hernández-Molina, F.J., Sierro, F.J., Bahr, A., Galvani, A., Lourens, L.J., Pardo-Igúzquiza, E., Pezard, P., Rodríguez-Tovar, F.J. 2016. Quaternary chronostratigraphic framework and sedimentary processes for the Gulf of Cadiz and Portuguese Contourite Depositional Systems derived from Natural Gamma Ray records. *Mar. Geol.*, 377, 40-57.
- Louarn, E. and Morin, P. 2011. Antarctic intermediate water influence on Mediterranean Sea water outflow. *Deep-Sea Res. Part II Topical Stud. Oceanog.*, 58(9), 932-942.
- Lowe, D.R. 1982. Sediment gravity flows; II, Depositional models with special reference to the deposits of high-density turbidity currents. *J. Sed. Res.*, 52(1), 279-297.
- Lozano, P., Fernández-Salas, L. M., Hernández-Molina, F. J., Sánchez-Leal, R., Sánchez-Guillamón, O., Palomino, D., Fariás, C., Mateo-Karrié, A., López-Gonzalez, N., García, M., Vázquez, J. T. 2020. Multiprocess interaction shaping geofoms and controlling substrate types and benthic community distribution in the Gulf of Cádiz. *Mar. Geol.*, 423, 106139.
- Maldonado, A., Somoza, L., Pallarés, L. 1999. The Betic orogen and the Iberian–African boundary in the Gulf of Cadiz: geological evolution (central North Atlantic). *Mar. Geol.*, 155(1-2), 9-43.
- Marchès, E., Mulder, T., Cremer, M., Bonnel, C., Hanquiez, V., Gonthier, E., Lecroart, P. 2007. Contourite drift construction influenced by capture of Mediterranean Outflow Water deep-sea current by the Fortimão submarine canyon (Gulf of Cadiz, South Portugal). *Mar. Geol.*, 242(4), 247-260.
- Malarkey, J., Baas, J. H., Hope, J. A., Aspdén, R. J., Parsons, D. R., Peakall, J., Paterson, D.M., Schindler, R.J., Ye, L., Lichtman, I.D., Bass, S.J., Davies, A.G., Manning, A.J., Thorne, P.D. 2015. The pervasive role of biological cohesion in bedform development. *Nature communications*, 6(1), 1-6.
- Martins, L.R. 2003. Recent sediments and grain-size analysis. *Gravel*, 1, 90-105.
- Martín-Chivelet, J., Fregenal-Martínez, M.A., Chacón, B. 2008. Traction structures in contourites. In: Rebesco, M., Camerlenghi, A. (Eds.), Contourites. *Developments in Sedimentology*, 60, 157-182.

- Matthew, A.J., Woods, A.J., Oliver, C. 1991. Spots before the eyes: new comparison charts for visual percentage estimation in archaeological material. Recent developments in ceramic petrology, 81, 211-263.
- Medialdea, T., Vegas, R., Somoza, L., Vázquez, J.T., Maldonado, A., Díaz-del-Río, V., Maestro, A., Córdoba, D., Fernández-Puga, M.C. 2004. Structure and evolution of the “Olistostrome” complex of the Gibraltar Arc in the Gulf of Cádiz (eastern Central Atlantic): evidence from two long seismic cross-sections. *Mar. Geol.*, 209(1-4), 173-198.
- Medialdea, T., Somoza, L., Pinheiro, L.M., Fernández-Puga, M.C., Vázquez, J.T., León, R., Ivanov, M.K., Magalhaes, V., Díaz-del-Río, V., Vegas, R. 2009. Tectonics and mud volcano development in the Gulf of Cádiz. *Mar. Geol.*, 261(1-4), 48-63.
- Meiburg, E., Kneller, B. 2010. Turbidity currents and their deposits. *Annual Review of Fluid Mechanics*, 42, 135-156.
- Mestdagh, T., Lobo, F.J., Llave, E., Hernández-Molina, F.J., van Rooij, D. 2019. Review of the late Quaternary stratigraphy of the northern Gulf of Cadiz continental margin: New insights into controlling factors and global implications. *Earth Sci. Rev.*, 198, p.102944.
- Middleton, G.V. and Hampton, M.A. 1973. Sediment gravity flows: mechanics of flow and deposition. In Middleton, G.V., and Bouma, A.H. (eds.), *Turbidity and Deep-Water Sedimentation*. SEPM, Pacific Section, Short Course Lecture Notes, Anaheim, 1-38.
- Migeon, S., Savoye, B., Zanella, E., Mulder, T., Faugeres, J. C., Weber, O. 2001. Detailed seismic and sedimentary study of turbidite sediment waves on the Var sedimentary ridge (SE France): significance for sediment transport and deposition and for the mechanism of sediment wave construction. *Mar. Pet. Geol.*, 18, 179–208.
- Miguez-Salas, O. and Rodríguez-Tovar, F.J. 2019. Ichnofacies distribution in the Eocene-Early Miocene Petros Tou Romiou outcrop, Cyprus: sea level dynamics and palaeoenvironmental implications in a contourite environment. *International Journal of Earth Sciences*, 108, 506-514.
- Miguez-Salas, O., Dorador, J. and Rodríguez-Tovar, F.J. 2019. Introducing Fiji and ICY image processing techniques in ichnological research as a tool for sedimentary basin analysis. *Marine Geology*, 413, 1-9.
- Millot, C., Candela, J., Fuda, J.L., Tber, Y. 2006. Large warming and salinification of the Mediterranean outflow due to changes in its composition. *Deep-Sea Res. Part I Topical Stud. Oceanogr.*, 53(4), 656-666.

- Miramontes E., Eggenhuisen J.T., Poneti, G., Silva Jacinto, R., Pohl, F., Hernández-Molina F.J. 2020. Channel-levee evolution in combined contour current–turbidity current flows from flume-tank experiments. *Geology*, 48 (4), 353–357.
- Mitchum, R.M., Vail, P.R., Sangree, J.B. 1977. Stratigraphic interpretation of seismic reflection patterns in depositional sequences. In: Payton, C. E. (Ed.), *Seismic Stratigraphy-Application to Hydrocarbon Exploration*, *AAPG Mem.* 26, 117–133.
- Mulder, T., Migeon, S., Savoye, B., Faugères, J.C., 2001. Inversely-graded turbidite sequences in the deep Mediterranean. A record of deposits by flood-generated turbidity currents. *Geo-Mar. Lett.*, 21 (2), 86–93.
- Mulder, T., Migeon, S., Savoye, B., Faugères, J.-C. 2002. Inversely- graded turbidite sequences in the deep Mediterranean. A record of deposits from flood-generated turbidity currents? A reply. *Geo-Marine Letters*, 22(2), 112–120.
- Mulder, T., Syvitski, J.P., Migeon, S., Faugeres, J.C., Savoye, B. 2003. Marine hyperpycnal flows: initiation, behavior and related deposits. A review. *Mar. Petrol. Geol.*, 20(6-8), 861-88.
- Mulder, T., Faugères, J.C., Gonthier, F. 2008. Mixed turbidite–contourite systems. In: Rebesco, M., Camerlenghi, A. (Eds.), *Contourites. Developments in Sedimentology*, 60, 435-456.
- Mulder, T. 2011. Gravity Processes and Deposits on Continental Slope, Rise and Abyssal Plains. In: *Deep-Sea Sediments* (Heiko Hüneke, Thierry Mulder, Eds.). *Developments in Sedimentology*, 63, 25-148.
- Mulder, T. and Hüneke, H. 2014. Turbidite. *Encyclopedia of Marine Geosciences*, 1-7.
- Mutti, E. 1990. Relazioni tra stratigrafia sequenziale e tettonica In: Atti del 75simo congresso nazionale della Società Geologica Italiana 'La Geologia Italiana degli Anni 90'. *Mem. della Soc. Geol. Ital. Rome, Italy, Soc. Geol. Ital.* 45, 627–655.
- Mutti, E. 1992. Turbidite sandstones. Agip, Istituto di geologia, Università di Parma.
- Mutti, E., Tinterri R., Remacha, E., Mavilla, N., Angella, S., Fava, F. 1999. An introduction to the analysis of ancient turbidite basins from an outcrop perspective, AAPG continuing education course note series # 39, Tulsa, Oklahoma, 61.
- Mutti, E., Ricci Lucchi, F., Roveri, M. 2002. Revisiting turbidites of the Marnoso-arenacea formation and their basin-margin equivalents: problems with classic models. *Excursion guidebook of the turbidite workshop*, Parma, Italy, 21–22.

- Mutti, E., Bernoulli, D., Lucchi, F. R., Tinterri, R. 2009. Turbidites and turbidity currents from Alpine 'flysch' to the exploration of continental margins. *Sedimentology*, 56(1), 267-318.
- Mutti, E. and Carminatti, M. 2012. Deep-water sands of the Brazilian offshore basins: Search and Discovery. In *AAPG Annual Convention & Exhibition*.
- Mutti, E., Cunha, R.S., Bulhoes, E.M., Arienti, L.M. and Viana, A.R. 2014. Contourites and turbidites of the Brazilian marginal basins. In *AAPG Annual Convention & Exhibition*.
- Mutti, E. (2019). Thin-bedded plumites: an overlooked deep-water deposit. *J. Mediterr. Earth Sci.*, 11.
- Nelson, C.H., Baraza, J., Maldonado, A. 1993. Mediterranean undercurrent sandy contourites, Gulf of Cadiz, Spain. *Sedimentary Geology*, 87(1-4), 103-131.
- Nishida, N. 2016. Microstructure of muddy contourites from the Gulf of Cádiz. *Mar. Geol.* 377, 110-117.
- Ochoa J. and Bray, N.A. 1991. Water mass exchange in the Gulf of Cadiz. *Deep-Sea Res.*, 38(1), S465-S503.
- Palamenghi, L., Keil, H., Spiess, V. 2015. Sequence stratigraphic framework of a mixed turbidite-contourite depositional system along the NW slope of the South China Sea. *Geo-Mar. Lett.*, 35(1), 1-21.
- Prather, B. E. 2003. Controls on reservoir distribution, architecture and stratigraphic trapping in slope settings. *Mar. Petrol. Geol.*, 20(6-8), 529-545.
- Peakall, J., McCaffrey, B., Keller, B. 2000. A process model for the evolution, morphology, and architecture of sinuous submarine channels. *J. Sediment. Res.*, 70, 434-448.
- Peakall, J., Best, J., Baas, J. H., Hodgson, D. M., Clare, M. A., Talling, P. J., Dorrel, R.M., Lee, D. R. 2020. An integrated process-based model of flutes and tool marks in deep-water environments: Implications for palaeohydraulics, the Bouma sequence and hybrid event beds. *Sedimentology*, 1601-1666.
- Postma, G. 1986. Classification of sediment gravity flow deposits based on flow conditions during sedimentation. *Geology*, 14, 291 – 294.
- Pratson, L.F. and Haxby, W.F. 1996. What is the slope of the US continental slope? *Geology*, 24(1), 3-6.
- Rebesco, M. and Stow, D.A.V. 2001. Seismic expression of contourites and related deposits: a preface. *Mar. Geophys. Res.*, 22(5-6), 303-308.
- Rebesco, M. 2005. Sedimentary environments contourites, in *Encyclopedia of Geology*, Elsevier, Oxford, pp. 513-527.

- Rebesco, M., Hernández-Molina, F. J., Van Rooij, D., Wåhlin, A. 2014. Contourites and associated sediments controlled by deep-water circulation processes: state-of-the-art and future considerations. *Mar. Geol.*, 352, 111–154.
- Richter, T.O., van der Gaast, S., Koster, B., Vaars, A., Gieles, R., de Stigter, H.C., De Haas, H., van Weering, T.C.E. 2006. The Avaatech XRF Core Scanner: technical description and applications to NE Atlantic sediments, *Geol. Soc. Spec. Publ.*, 267, 39-50.
- Rider, M., Kennedy, M. 2011 The geological interpretation of well logs.
- Rodríguez-Tovar, F.J. and Hernández-Molina, F.J. 2018. Ichnological analysis of contourites: Past, present and future. *Earth Sci. Rev.*, 182, 28-41.
- Rodríguez-Tovar, F.J. and Dorador, J. 2014. Ichnological analysis of Pleistocene sediments from the IODP Site U1385 “Shackleton Site” on the Iberian Margin: approaching palaeoenvironmental conditions. *Palaeogeogr. Palaeoclimatol. Palaeoecol.*, 409, 24–32.
- Rodríguez-Tovar, F.J. and Uchman, A. 2004. Trace fossil after the K-T boundary event from the Agost section, SE Spain. *Geol. Mag.*, 141, 429-449.
- Rodríguez-Tovar, F.J. and Uchman, A. 2006. Ichnological analysis of the Cretaceous-Palaeogene boundary interval at the Caravaca section, SE Spain. *Palaeogeogr. Palaeoclimatol. Palaeoecol.*, 242, 311-355.
- Rodríguez-Tovar, F.J., Uchman, A., Martín-Algarra, A. 2009. Oceanic anoxic event at the Cenomanian-Turonian boundary interval (OAE-2): ichnological approach from the Betic Cordillera, southern Spain. *Leina*, 42, 407-417.
- Rodríguez-Tovar, F.J., Dorador, J., Martín-García, G.M., Sierro, F.J., Flores, J.A., Hodell, D.A. 2015a. Response of macrobenthic and foraminifer communities to changes in deep-sea environmental conditions from marine isotope stage (MIS) 12 to 11 at the “Shackleton Site”. *Glob. Planet. Chang.*, 133, 176-187.
- Rodríguez-Tovar, F.J., Dorador, J., Grunert, P., Hodell, D. 2015b. Deep-sea trace fossil and benthic foraminiferal assemblages across glacial terminations 1, 2 and 4 at the “Shackleton Site” (IODP Expedition 339, Site U1385). *Glob. Planet. Chang.*, 133, 359-370.
- Rodríguez-Tovar, F.J., Hernández-Molina, F.J., Hüneke, H., Chiarella, D., Llave, E., Mena, A., Miguez-Salas, O., Dorador, J., de Castro, S. Stow, D.A.V. 2019a. Key evidence for distal turbiditic and bottom-current interactions from tubular turbidite infills. *Palaeogeogr. Palaeoclimatol. Palaeoecol.*, 109-233.

- Rodríguez-Tovar, F.J., Hernández-Molina, F.J., Hüneke, H., Llave, E., Stow, D. 2019b. Contourite facies model: Improving contourite characterization based on the ichnological analysis. *Sedimentary Geology*, 384, 60-69.
- Rogerson, M., Bigg, G.R., Rohling, E.J., Ramirez, J. 2012. Palaeoceanography of the Atlantic-Mediterranean exchange: overview and first quantitative assessment of climatic forcing. *Reviews of Geophysics*, 50.
- Roque, C., Duarte, H., Terrinha, P., Valadares, V., Noiva, J., Cachão, M., Ferreira, J., Legoinha, P., Zitellini, N. 2012. Pliocene and Quaternary depositional model of the Algarve margin contourite drifts (Gulf of Cadiz, SW Iberia): seismic architecture, tectonic control and paleoceanographic insights. *Mar. Geol.*, 303, 42-62.
- Rothwell, R.G., Hoogakker, B., Thomson, J., Croudace, I.W., Frenz, M. 2006. Turbidite emplacement on the southern Balearic Abyssal Plain (western Mediterranean Sea) during Marine Isotope Stages 1–3: an application of ITRAX XRF scanning of sediment cores to lithostratigraphic analysis. Geological Society, London, Special Publications, 267(1), 79-98.
- Sánchez-Leal, R.F., Bellanco, M.J., Fernández-Salas, L.M., García-Lafuente, J., Gasser-Rubinat, M., González-Pola, C., Hernández-Molina, F.J., Pelegrí, J.L., Peliz, A., Relvas, Roque, D. 2017. The Mediterranean Overflow in the Gulf of Cadiz: A rugged journey. *Sci. Adv.*, 3(11), 1-11.
- Sanders, J.E. 1965. Primary sedimentary structures formed by turbidity currents and related resedimentation mechanisms. In Middleton, G. V. (ed.), *Primary Sedimentary Structures and their Hydrodynamic Interpretation*. Tulsa: *SEPM. Spec. Publ.*, 12, 192–219.
- Sansom, P. 2018. Hybrid turbidite–contourite systems of the Tanzanian margin. *Pet. Geosci.*, 24(3), 258-276.
- Schönfeld J., Zahn, R. 2000 Late Glacial to Holocene history of the Mediterranean Outflow. Evidence from benthic foraminiferal assemblages and stable isotopes at the Portuguese margin. *Palaeogeogr. Palaeoclimatol. Palaeoecol.*, 159, 85-111.
- Schönfeld J., Zahn R., Abreu L. 2003. Surface and deep-water response to rapid climate changes at the Western Iberian Margin. *Global Planet Change*, 36, 237-264.
- Serra, O. and Sulpice, L. 1975. Sedimentological analysis of shale-sand series from well logs. In *SPWLA 16th Annual Logging Symposium*. Society of Petrophysicists and Well-Log Analysts.
- Serra, O. 1985. Sedimentary environments from wireline logs. Schlumberger Limited.

- Shanmugam, G. 2000. 50 years of the turbidite paradigm (1950s-1990s): deep-water processes and facies models—a critical perspective. *Mar. Petrol. Geol.*, 17(2), 285-342.
- Shanmugam, G. 2008. Deep-water bottom currents and their deposits, in: Rebesco, M., Camerlenghi (Eds.), *Contourites. Developments in Sedimentology*, 60, 59-81.
- Shanmugam, G., Spalding, T.D., Rofheart, D.H. 1993. Traction structures in deep-marine, bottom-current-reworked sands in the Pliocene and Pleistocene, Gulf of Mexico. *Geology*, 21(10), 929-932.
- Shanmugam, G. 2012. New perspectives on deep-water sandstones: origin, recognition, initiation, and reservoir quality. *Handbook of Petroleum Exploration and Production*, vol. 9. Elsevier, Amsterdam, p. 524.
- Shanmugam, G. 2013. New perspectives on deep-water sandstones: implications. *Petrol. Explor. Dev.*, 40, 316-324.
- Sierro, F.J., Flores, J.T., Baraza, J. 1999. Late glacial to recent paleoenvironmental changes in the Gulf of Cadiz and formation of sandy contourite layers. *Mar. Geol.*, 155(1-2), 157-172.
- Somoza, L., Díaz del Río, V., León, R., Ivanov, M., Fernández-Puga, M.C., Gardner, J.M., Hernández-Molina, F.J., Pinheiro, L.M., Rodero, J., Lobato, A. Maestro, A. 2003. Seabed morphology and hydrocarbon seepage in the Gulf of Cadiz mud volcano area: Acoustic imagery, multibeam and ultra-high resolution seismic data. *Mar. Geol.*, 195(1-4), 153-176.
- Stanley, D.J. 1987. Turbidite to current-reworked sand continuum in Upper Cretaceous rocks, U.S. Virgin Islands, *Mar. Geol.*, 78, 143-151.
- Stanley, D.J. 1988. Turbidites reworked by bottom currents: upper cretaceous examples from St. Croix, US Virgin Islands. *Smithsonian contributions to the marine sciences. Mar. Sci.*, 33, pp. 85.
- Stanley, D.J. 1993. Model for turbidite-to-contourite continuum and multiple process transport in deep marine settings: examples in the rock record. *Sed. Geol.*, 82(1-4), 241-255.
- Stow, D.A.V. 1979. Laurentian Fan--Deep-Sea Fan Models, Fine-Grained Sediment Distribution, and Hydrocarbon Exploration. *AAPG Bulletin*, 63(3), 535-535.
- Stow, D.A.V. 1982. Bottom currents and contourites in the North Atlantic. *Bull. Inst. Geol. Bassin Aquitaine*, 31, 151-166.
- Stow, D. A., Wetzel, A. 1990. Hemiturbidite: a new type of deep-water sediment. In *Proceedings of the ocean drilling program, scientific results. Ocean Drilling Program College Station, TX*, 116, 25-34.

- Stow, D.A.V. Faugères, J.C. 1998. Contourites, turbidites and process interaction. *Sediment. Geol.*, 115, 1–386.
- Stow, D.A.V., Faugères, J.C., Howe, J.A., Pudsey, C.J., Viana, A.R. 2002. Bottom currents, contourites and deep-sea sediment drifts: current state-of-the-art. *Geo. Soc. London Memo.*, 22(1), 7-20.
- Stow, D.A.V., Hunter, S., Wilkinson, D., Hernández-Molina, F.J. 2008. The nature of contourite deposition. In: Rebesco, M., Camerlenghi, A. (Eds.), *Contourites. Developments in sedimentology*, 60, 143-156.
- Stow, D.A.V., Hernández-Molina, F.J., Llave, E., Bruno, M., García, M., Díaz del Río, V., Somoza, L., Brackenridge, R.E. 2013a. The Cadiz Contourite Channel: Sandy contourites, bedforms and dynamic current interaction. *Mar. Geol.*, 34, 99-114.
- Stow, D.A.V., Hernández-Molina, F.J., Alvarez Zarikian, C.A., Expedition 339 Scientists. 2013b. Proceedings IODP, 339. Integrated Ocean Drilling Program Management International, Tokyo.
- Stow, D., Smillie, Z. 2020. Distinguishing between Deep-Water Sediment Facies: Turbidites, Contourites and Hemipelagites. *Geosciences*, 10(2), 68.
- Talling, P.J., Masson, D.G., Sumner, E., Malgesini, G. 2012. Subaqueous sediment density flows: Depositional processes and deposit types. *Sedimentology*, 59(7), 1937-2003.
- Tallobre, C., Giresse, P., Bassetti, M.A., Loncke, L., Bayon, G., Buscail, R., Tudryn, A., Zaragosi, S. 2019. Formation and evolution of glauconite in the Demerara Contourite depositional system related to NADW circulation changes during late Quaternary (French Guiana). *J. S. Am. Earth. Sci.* 92, 167-183.
- Terrinha, P., Matias, L., Vicente, J., Duarte, J., Luis, J., Pinheiro, L., Lourenço, N., Diez, S., Rosas, F., Magalhães, V., Valadares, V., Zitellini, N., Roque, C., Mendes Victor, L., MATESPRO Team. 2009. Morphotectonics and strain partitioning at the Iberia–Africa plate boundary from multibeam and seismic reflection data. *Mar. Geol.*, 267(3-4), 156-174.
- Thomson, J., Mercone, D., De Lange, G.J., Van Santvoort, P.J.M., 1999. Review of recent advances in the interpretation of eastern Mediterranean sapropel S1 from geochemical evidence. *Mar. Geol.* 153 (1–4), 77–89.
- Thomson, J., Crudeli, D., De Lange, G. J., Slomp, C. P., Erba, E., Corselli, C. T., Calvert, S. E. 2004. *Florisphaera profunda* and the origin and diagenesis of carbonate phases in eastern Mediterranean sapropel units. *Paleoceanography*, 19(3).

- Viana, A.R., Almeida, W., Nunes, M.C.V. and Bulhões, E.M. 2007. The economic importance of contourites. *Geol. Soc. London Spec. Publ.* 276(1), 1-23.
- Viana, A.R. 2008. Economic relevance of contourites. In: Rebesco, M., Camerlenghi, A. (Eds.), *Contourites. Developments in Sedimentology*, 60. Elsevier, Amsterdam, 493-510.
- Voelker, A.H.L., Lebreiro, S.M., Schönfeld, J., Cacho, I., Erlenkeuser, H., and Abrantes, F. 2006. Mediterranean Outflow strengthening during Northern Hemisphere coolings: a salt source for the glacial Atlantic? *Earth Planet. Sci. Lett.*, 245(1–2):39–55.
- Wang, X., Zhuo, H., Wang, Y., Mao, P., He, M., Chen, W., Zhou, J., Gao, S., Wang, M. 2018. Controls of contour currents on intra-canyon mixed sedimentary processes: Insights from the Pearl River Canyon, northern South China Sea. *Mar. Geol.*, 406, 193-213.
- Wu, X., Baas, J. H., Parsons, D. R., Eggenhuisen, J., Amoury, L., Cartigny, M., McLelland, S., Mouazé, D., Ruessink, G. 2018. Wave Ripple Development on Mixed Clay- Sand Substrates: Effects of Clay Winnowing and Armoring. *J. Geophys. Res. Earth Surf.*, 123(11), 2784-2801.

Table captions

Table 1. Summary of sedimentary sequence datasets from Sites U1389 and U1388. Sedimentary sequences interpreted by this study are marked in bold.

Site, Hole, Section	mbsf (base)	mcd (base)	Length (cm)	Preservation	XRF	Grain Size	Thin section	SEM
U1388 B 4Xcc	28.68	28.68	24	Incomplete (Top-bottom missing)	no	no	no	no
U1388 B 9Xcc	74.18	74.18	32	Incomplete (Top-bottom missing)	no	no	no	no
U1388 B 19X1	168.28	168.28	0	Incomplete (Top missing)	no	no	no	no
U1388 B 20X5	184.78	184.78	156	Complete	yes	yes	From bottom to top	no
U1388 B 21X1	187.56	187.56	16	Washed	no	no	no	no
U1388 B 21Xcc	188.83	188.83	19	Incomplete (Bottom missing)	no	no	no	no
U1389 A 27X6-7	244.02	273.88	30	Complete	yes	yes	Some intervals	F3 and F4 (Microtexture)
U1389 A 28X6-7	254.33	286.47*	87	Complete	yes	yes	Some intervals	F3 and F4 (Microtexture)
U1389 A 35X2	314.23	361.33**	42	Complete	yes	yes	Some intervals	F1 and F5 (Microstructure)
U1389 A 35X3	315.57	362.70	37	Incomplete (Bottom missing)	no	no	no	no
U1389 A 35Xcc	320.64	367.77	25	Incomplete (Bottom missing)	no	no	Some intervals	F3 and F4 (Microtexture)
U1389 A 36Xcc	324.47	371.70	23	Incomplete (Top-bottom missing)	no	no	no	no
U1389 A 37X3	334.66	380.00	26	Incomplete (Top missing)	no	no	no	no

U1389 A 37Xcc	336.48	381.24	24	Incomplete (Top- bottom missing)	no	no	Some intervals	no
U1389 A 39X1	349.70	389.15	12	Incomplete (Top missing)	no	no	Some intervals	no
U1389 C 28X2	251.55	286.64*	35	Incomplete (washed top missing)	no	no	no	no
U1389 C 32X4	293.99	332.38	43	Complete	yes	yes	From bottom to top	F1 and F5 (Microstructure)
U1389 C 35X3	320.58	361.49**	75	Complete	yes	yes	yes	F3 and F4 (Microtexture)

Table 2. Correlation matrix for XRF analyses. Bold: $r > 0.7$ and $r < -0.7$ (highly correlated), light grey: $0.7 < r < 0.2$ (slightly correlated), dashed: $0.2 < r < -0.2$ (not correlated). Variables (elemental peak area cps) have been standardized to their means and standard deviations.

	<i>Al</i>	<i>Si</i>	<i>K</i>	<i>Ca</i>	<i>Ti</i>	<i>Mn</i>	<i>Fe</i>	<i>Br</i>	<i>Rb</i>	<i>Sr</i>
Si	0.640									
K	0.964	0.581								
Ca	-0.918	-0.692	-0.915							
Ti	0.937	0.627	0.941	-0.956						
Mn	-	0.475	-	-0.332	0.245					
Fe	0.905	0.563	0.900	-0.961	0.932	0.272				
Br	0.587	-	0.664	-0.555	0.587	-	0.600			
Rb	0.821	0.556	0.870	-0.879	0.868	0.212	0.854	0.595		
Sr	-0.843	-0.641	-0.868	0.829	-0.836	-	-0.763	-0.433	-0.694	
Zr	-	-	-	-	-	0.273	-	-	-	-

Figure captions

Figure 1. A) Gulf of Cadiz showing the pathway of Mediterranean Outflow water (MOW; white arrows) after it exits the Strait of Gibraltar. The IODP Exp. 339 Site (U1386-U1390) locations are indicated by black dots. Contourite Depositional System: 1= proximal scour and sand-ribbon sector, 2= overflow-sedimentary lobe sector, 3= channels and ridges sector, 4= contourite deposition sector and 5= submarine canyon sector (Adapted from Hernández-Molina et al., 2003, 2006). Black box represents the exact location of isochrons maps from Fig. 2. B) Circulation of the Mediterranean Outflow water (MOW) along the Gulf of Cadiz middle slope with the present-day interplay of along- and down- slope processes. The ML is divided into five branches: Southern Branch, Western Branch, Central Branch, Northern Branch, and Eastern Branch (modified after García et al. 2009). Map shows the position of the diapiric

ridges and marginal valleys. Legend for seafloor features: CC= Contouritic Channel; DR= Diapiric Ridge. C) Map indicating the position of the contourite channels, location of the seismic grid used in this study (Fig. 2), Sites U1388 and U1389 drilled during IODP Exp. 339.

Figure 2. A) Seismic profile (Line HE 91-20) across Site U1389 in the Doñana basin (Central sector) including the major discontinuities: Late Quaternary Discontinuity (LQD); Mid-Pleistocene Discontinuity (MPD), Early Quaternary Discontinuity (EQD), and seismic units (adapted from Hernández-Molina et al., 2016b). Profile location given in Fig. 1C. Legend for features: CC= Contouritic Channel; DR= Diapiric Ridge. Surface maps for discontinuities R4 (L) and MPD (C) show the distribution of the major structural elements in the study area around Site U1389 and Site U1388. These include down-slope valleys and depressions, structural highs (Guadalquivir bank, Betic and flysch units) and Guadalquivir and Cadiz diapiric ridges. D) Close-up from Fig. 2A showing ENE migration of Channel System I and truncation of v-shaped features (red discontinuous lines). E) Close-up of Channel System II from Fig. 2A. See the shape of u-shaped features and downlapping of oblique seismic reflections against previous deposits (red discontinuous lines). The two different u-shaped features are divided by the discontinuous orange lines. DR= Diapiric Ridge.

Figure 3. Correlation between line HE 91-20, Hole U1389E well log, and U1389A sedimentary log. Dark blue lines and shaded light blue area represent a close-up of the studied interval from 220 to 355 mbsf. For this interval, gamma-ray logs show two different colours: a) blue represents serrated gamma-ray logs interpreted as overspill deposits in subunit Q4 with the appearance of the sedimentary sequences, and b) dark yellow represents two funnel-shaped gamma-ray logs interpreted as Channel System II activity. Sedimentary sequences are indicated by orange rectangles.

Figure 4. Summary of the five facies identified as the sedimentary sequence including a sketch (not to scale) of vertical association of facies, texture, microfacies, sedimentary features, and grain size parameters. The grain size distribution curves represent the average of measurements in each facies. Red boxes in the sketch indicate locations of thin-section samples with corresponding figure numbers. The black box in grain size distribution curves represents the sandy fraction. Legend for bioturbation: Pf= *Planolites*; Th= *Thalassinoides*.

Figure 5. (A-E) X-ray fluorescence elemental ratios ($\ln \text{Ca/Ti}$, $\ln \text{Ca/Sr}$, $\ln \text{Zr/Al}$) plotted against depth in high-resolution core images of sedimentary sequences. Shaded blue rectangles represent peaks in bottom current activity ($\ln \text{Zr/Al}$; Bahr et al., 2014, 2015). Coloured dots represent discrete sample locations related to each grain size distribution curve. The black box in grain size distribution curves represents the sandy fraction.

Figure 6. (A-G) High-resolution core images of the sedimentary sequences showing vertical facies associations, trace fossils, and bioturbation horizons. The coloured dots represent discrete sample locations for grain size analysis. White thin box in G indicates the location of the large-size thin-section sample from Figure 7A.

Figure 7. Sedimentary microfacies: A) Very large-size thin-section scan showing the vertical microfacies association of the sedimentary sequences interpreted as bottom current reworked sands (BCRS) (see Fig. 6G for location). Blue arrows indicate millimetre-scale discrete laminations of opaques concentrations. B) F4 to F5 microfacies grain-supported texture with an increase of matrix content and planktonic foraminifera. C) Gradual contact between F4 and F5 preserving quartz grain size and increase in matrix content. D) Detail of a F1 mud chip present in F2. E) Erosional contact between F1 and F2 and the presence of a F1 rip-up clast. Relative position of B, C, and E within the vertical sequence shown in Fig. 4.

Figure 8. SEM images showing common microstructures in F1 (A, B), in F4 (C) and in F5 (D). A) Minor plate-like (PL) silt particles are oriented parallel to bedding. B) and D) Silt grains (S) and randomly oriented (R) clay particles. C) F4 microtexture with residual matrix (M) attached to quartz grain surfaces. Red dots = subrounded quartz grains, blue dots = angular quartz grains.

Figure 9. Detailed micro-photograph and respective illustration of common bottom and top contacts of heterolithic textures present in F3 and F4 with full winnowed lamina (A), gradual matrix-rich to matrix-free upper and lower contact (B), sharp-base transitional upper matrix-free to matrix-rich contact (C), and very-thin matrix-free to matrix-rich intercalations (D). Yellow arrows indicate millimetre scale discrete laminations of opaques concentrations.

Figure 10. A) Cross-plot of kurtosis against D50 (mean grain size) shows that fine and very fine-grained sands (F3-F4) have a higher concentration of grain sizes around the mean whereas the finer and coarse-grained silts show a broader (platykurtic) distribution. B) D50 versus skewness. F1 includes a coarse-grained subpopulation while F4 shows a

very fine-grained skew distribution. C) D50 versus sorting reveals that F1 fine-grained silt and F5 fine-grained sands vary inversely with sorting. F2, F3, and F4 coarse-grained silt and fine-grained sand vary positively with sorting.

Figure 11. Plots of A) Skewness versus sorting and B) skewness versus kurtosis showing three main trends. Highlighted areas show trends (a-c) in grain size distribution curves for each facies. Grain size distribution changes in response to different sedimentary processes. See text for explanation.

Figure 12. Compositional plots for F1 to F5 facies showing Fe (A), Ca (B), Si (C), and Sr (D) versus Ti, (E) the relationships between carbonate content ($\ln \text{Ca/Ti}$) and bottom current intensity ($\ln \text{Zr/Al}$), and (F) association of carbonate ($\ln \text{Ca/Sr}$) and siliciclastic ($\ln \text{Si/Al}$) input. Cross-plots show three main trends denoted *a* for F1, *b* for F2 and F5, and *c* for F3 and F4. Data points are colour coded with respect to different facies.

Figure 13. Comparison of the classic turbidite Bouma Sequence (Bouma, 1962), contourite bi-gradational sequence (Gonthier et al., 1994; Faugères et al., 1984, later modified by Stow and Faugères, 2008), and the partial bi-gradational contourite sequences including BCRS as proposed in this study. Legend for grain size: fs = fine silt; cs = coarse silt; FS = Fine Sand.

Figure 14. A) Sketch of the sedimentary environment based on R4 and MPD isochore maps (Fig. 2B and 2C) and the distribution of geological and sedimentary features based on the seismic data set previously considered by Llave et al. (2007) and García et al. (2009). Conceptual sketch explaining the formation of partial bi-gradational contourite sequences including BCRS and as a conceptual depositional model for F1 – F5 facies observed in the cores (Not to scale). Relative position from sites U1389 and U1388 is included as well as the situation of the crossing profile from the Figure 16. The current position of Sites U1388 and U1389 has been included in the sketch, although the paleogeographic situation for the studied intervals with sequences including BCRS in the U1388 was also in the contourite channel – drift transition, and therefore similar to the U1389 location at present day. B-E). Scenario for the continuous development of facies associations and depositional processes with settling in grey, suspension in orange, traction in blue, and suspension in violet. F) Final sedimentary sequence with facies association observed (9).

Figure 15. Detailed sketch of the depositional model for the bottom current reworked sands (BCRS). A) F2 is deposited and bioturbated by *Planolites*. B) F2 is subjected to shear

stress by bottom currents. Shear stress gets progressively less efficient and F3 starts to develop (incipient ripples). C) The reworking and winnowing of the fine fraction caused a shear stress reduction through time and space, after a time span of prevalent erosion at a fixed site, F4 ripple interval begins to develop (Adapted from Gambacorta et al., 2014). D) After F4 deposition, bottom currents become weaker but remain active in pirating fine-grained fractions from dilute turbiditic currents forming F5.

Figure 16. Sketch of a crossing profile integrating the proposed partial bi-gradational contourite sequences including BCRS along the drift (closer to the adjacent contourite channel). Included its lateral relation with the standard contourite facies sequence on the drift proposed by Gonthier et al. (1984) and Faugères et al. (1984), and later modified by Stow and Faugères (2008), and the sandier sedimentary facies along the adjacent contourite channels described by Brackenridge et al. (2018).

Figure 17. Simple depositional model for a mixed system continental margin showing the position of the proposed partial bi-gradational contourite sequences including bottom current reworked sands (BCRS) and examples of reworked turbidites. Relative position for different BCRS (Shanmugam, 1993; Fuhrman et al., 2020), reworked turbidites (Stanley, 1987, 1988, 1993; Mutti, 1990; Gong et al., 2016; Sansom, 2018) and contourites (Gonthier et al., 1982; Viana et al., 2007; Mutti et al., 2014; Brackenridge et al., 2018; Hernández-Molina et al., 2018) is shown for comparison.

Highlights

- Sedimentological study of the interaction between down- and along-slope processes;
- A contourite drift containing reworked turbidites is described;
- Turbidites are subjected to reworking and winnowing by bottom currents;
- The sedimentary sequence is a novel example of a turbiditic remnant reworked by bottom currents within a contouritic drift;
- Contourite drifts are not only formed by contourite deposits;
- The vertical trend in the sedimentary sequence presented records long- and short- term variation in turbidite-contourite interactions.

Journal Pre-proof

Figure 1.

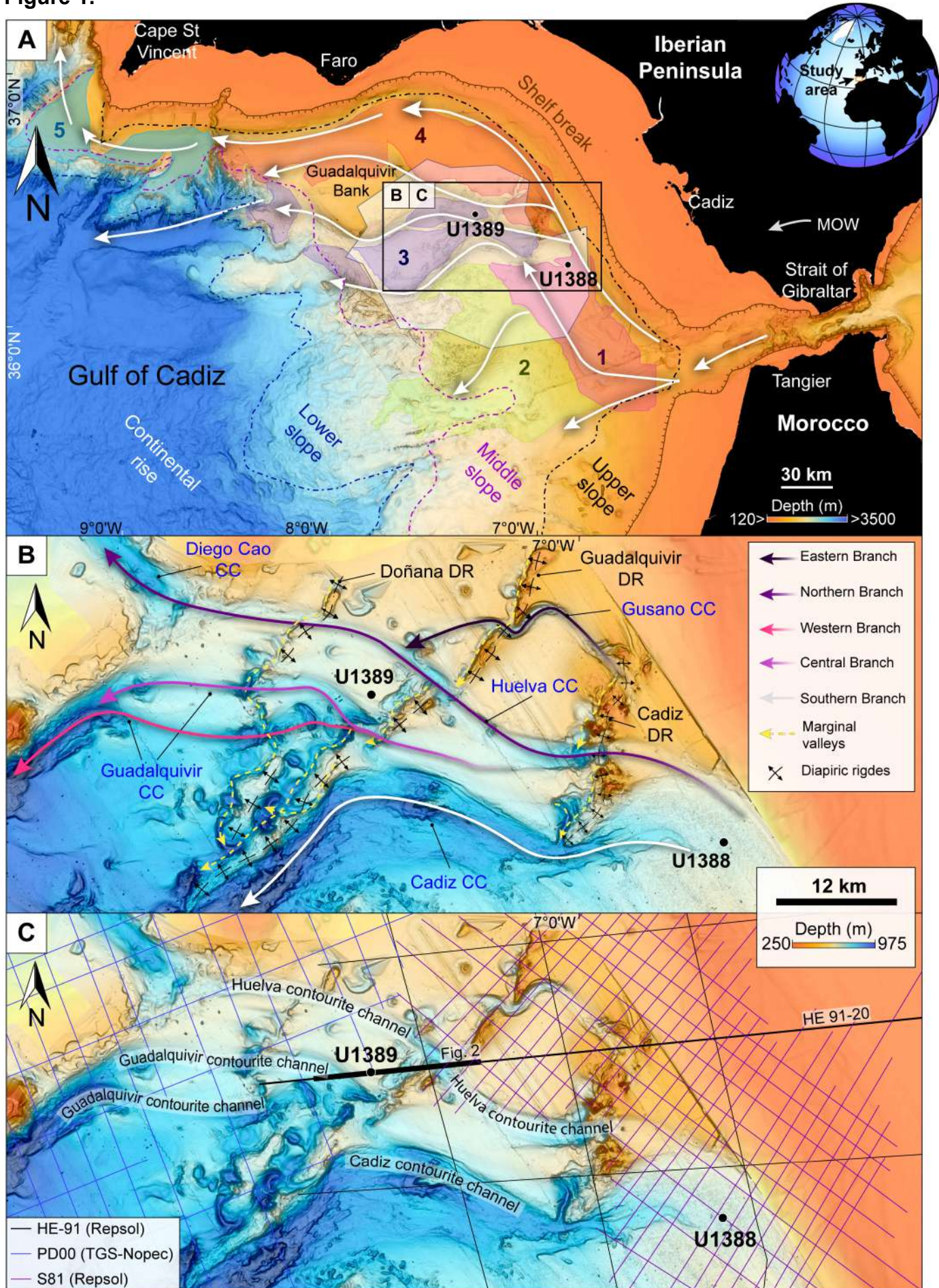


Figure 2.

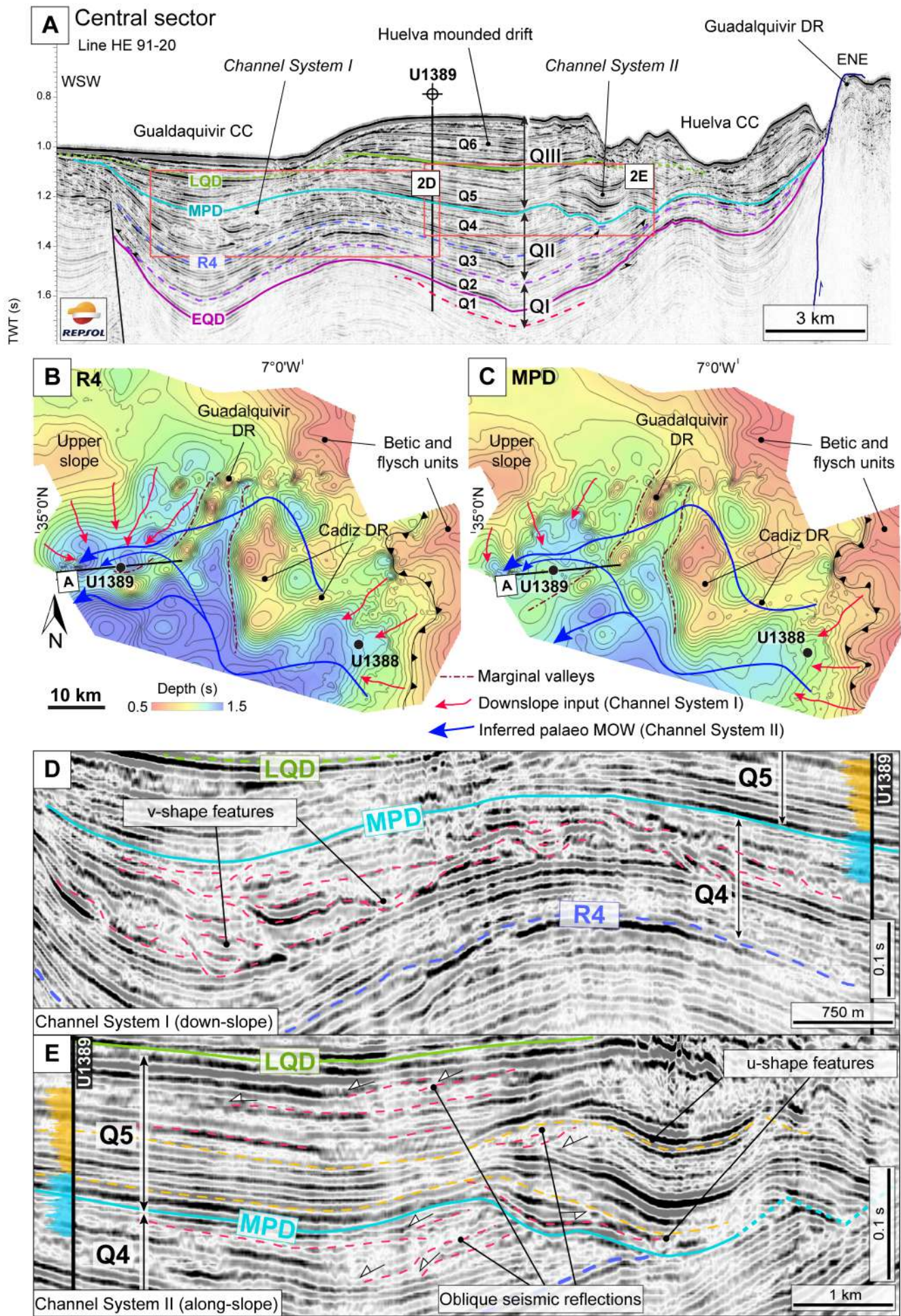


Figure 3.

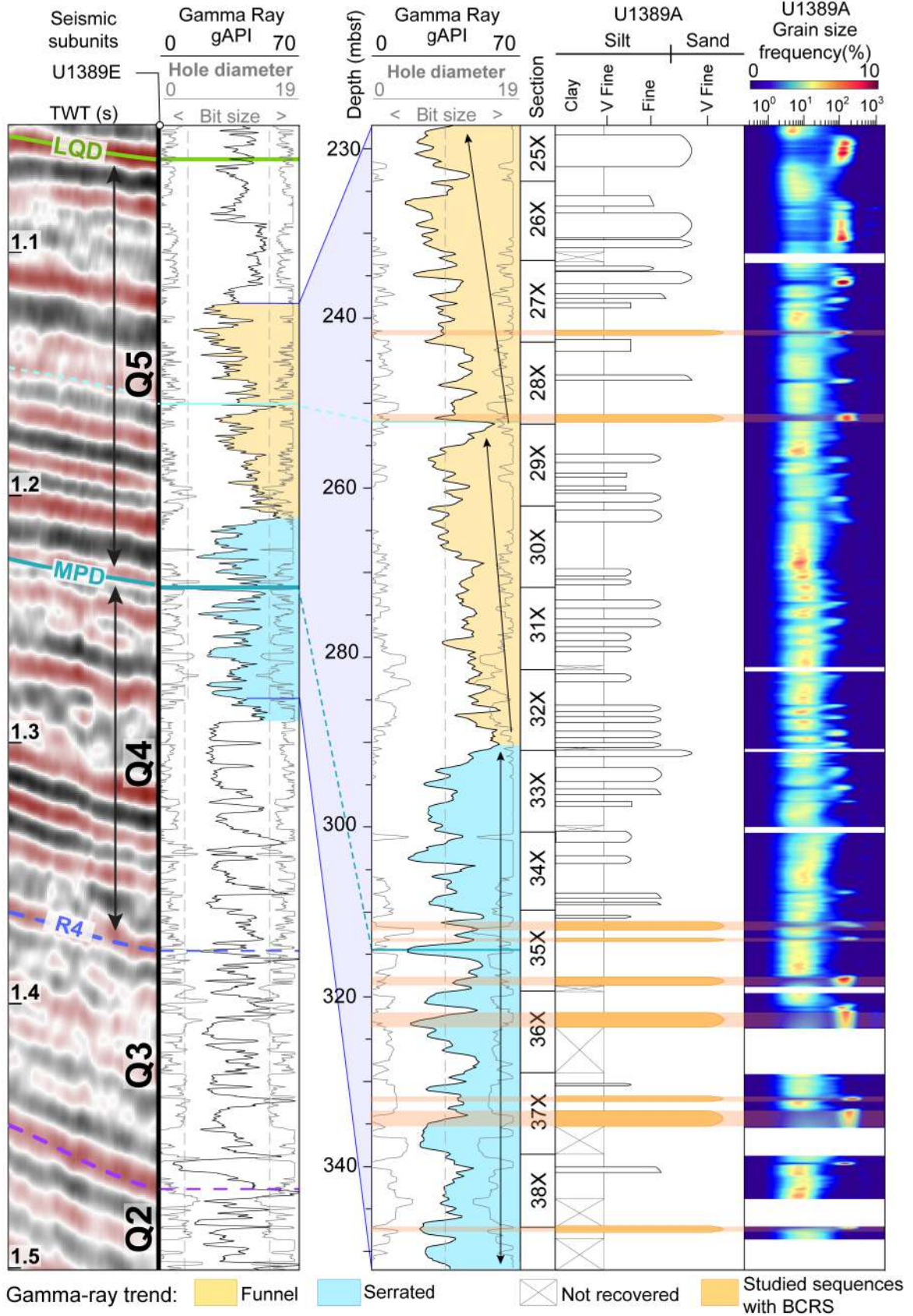


Figure 4.

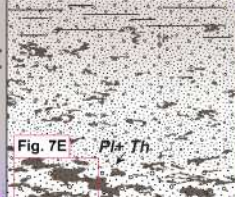

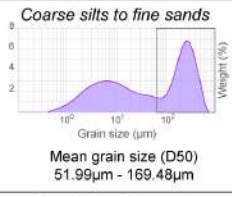
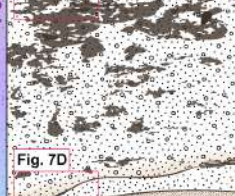

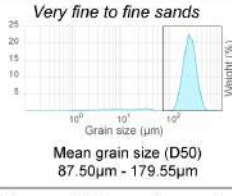
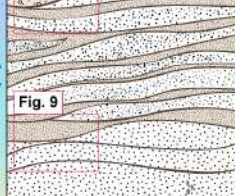

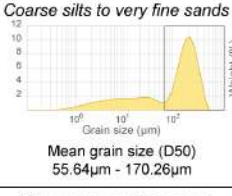
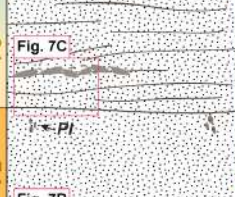

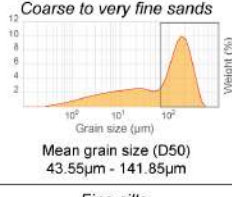
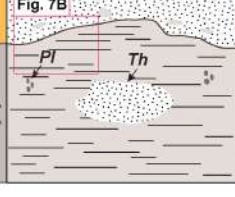

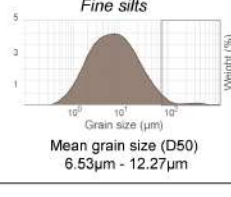
	SKETCH	FACIES	MICROFACIES	SEDIMENTARY FEATURES	GRAIN SIZE PARAMETERS
F1		FACIES 5 U1389A 35X2		Normally graded Mottled texture Fragmented shell remains Highly bioturbated Sharp/gradual base	SORTING: <i>Very poorly sorted</i> Max: 2.810 Min: 2.040 Avr: 2.508 SKEWNESS: <i>Very fine skewed</i> Max: 0.647 Min: 0.012 Avr: 0.429 KURTOSIS: <i>Platykurtic</i> Max: 1.593 Min: 0.642 Avr: 0.851  Sand 63.12 % Silt 32.62 % Clay 4.27 %
F5		FACIES 4 U1389C 32X4		Inversely graded Lenticular bedded Mud-rich mud-free alternations Scarce bioturbated Sharp/gradual base	SORTING: <i>Very poorly sorted to moderately sorted</i> Max: 2.500 Min: 0.860 Avr: 1.914 SKEWNESS: <i>Very fine skewed</i> Max: 0.652 Min: 0.363 Avr: 0.533 KURTOSIS: <i>Mesokurtic-Platykurtic</i> Max: 2.892 Min: 0.800 Avr: 1.112  Sand 68.27 % Silt 28.47 % Clay 3.27 %
F4		FACIES 3 U1389C 32X4		Massive Thin planar-laminated Mud-rich mud-free alternations Scarce bioturbated Sharp base	SORTING: <i>Very poorly sorted</i> Max: 2.810 Min: 2.529 Avr: 2.670 SKEWNESS: <i>Very fine skewed</i> Max: 0.606 Min: -0.012 Avr: 0.283 KURTOSIS: <i>Platykurtic</i> Max: 0.738 Min: 0.625 Avr: 0.678  Sand 63.20 % Silt 32.65 % Clay 4.1 %
F3		FACIES 2 U1389A 28X7		Massive/Normally graded Occasionally shell lags at the base Rip-up clasts Scarcely bioturbated Sharp base	SORTING: <i>Very poorly sorted</i> Max: 2.451 Min: 2.258 Avr: 2.348 SKEWNESS: <i>Very fine skewed</i> Max: 0.523 Min: 0.087 Avr: 0.358 KURTOSIS: <i>Platykurtic</i> Max: 0.793 Min: 0.714 Avr: 0.755  Sand 57.05 % Silt 38.77 % Clay 4.17 %
F2		FACIES 1 U1389A 35X2		Massive Occasionally bioturbated Sharp/gradual base	SORTING: <i>Poorly sorted</i> Max: 2.18 Min: 1.63 Avr: 1.87 SKEWNESS: <i>Symmetrical</i> Max: -0.03 Min: -0.08 Avr: -0.067 KURTOSIS: <i>Mesokurtic</i> Max: 1.028 Min: 0.867 Avr: 0.942  Sand 8.70 % Silt 79.33 % Clay 11.97 %

Figure 5.

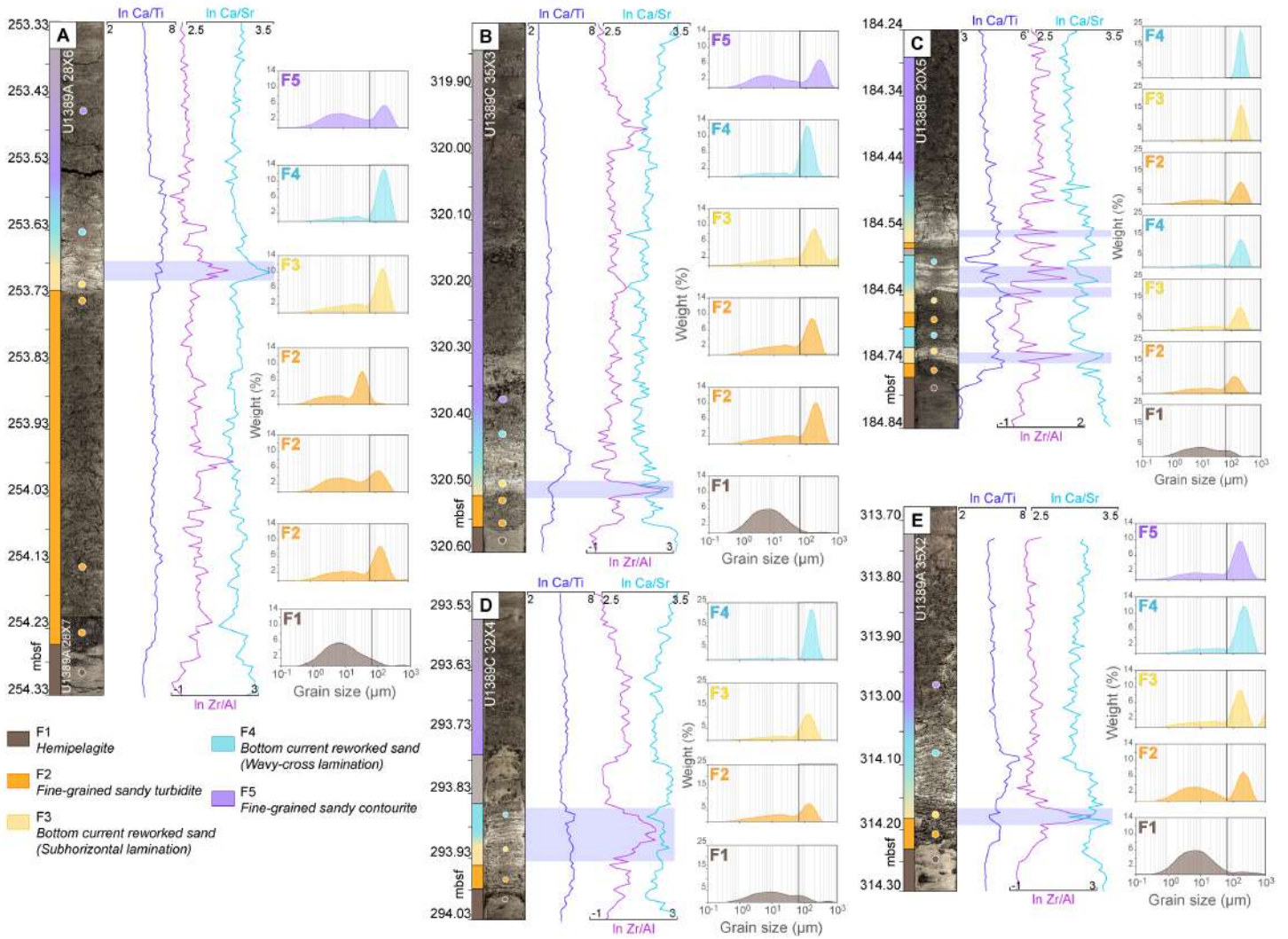


Figure 6.

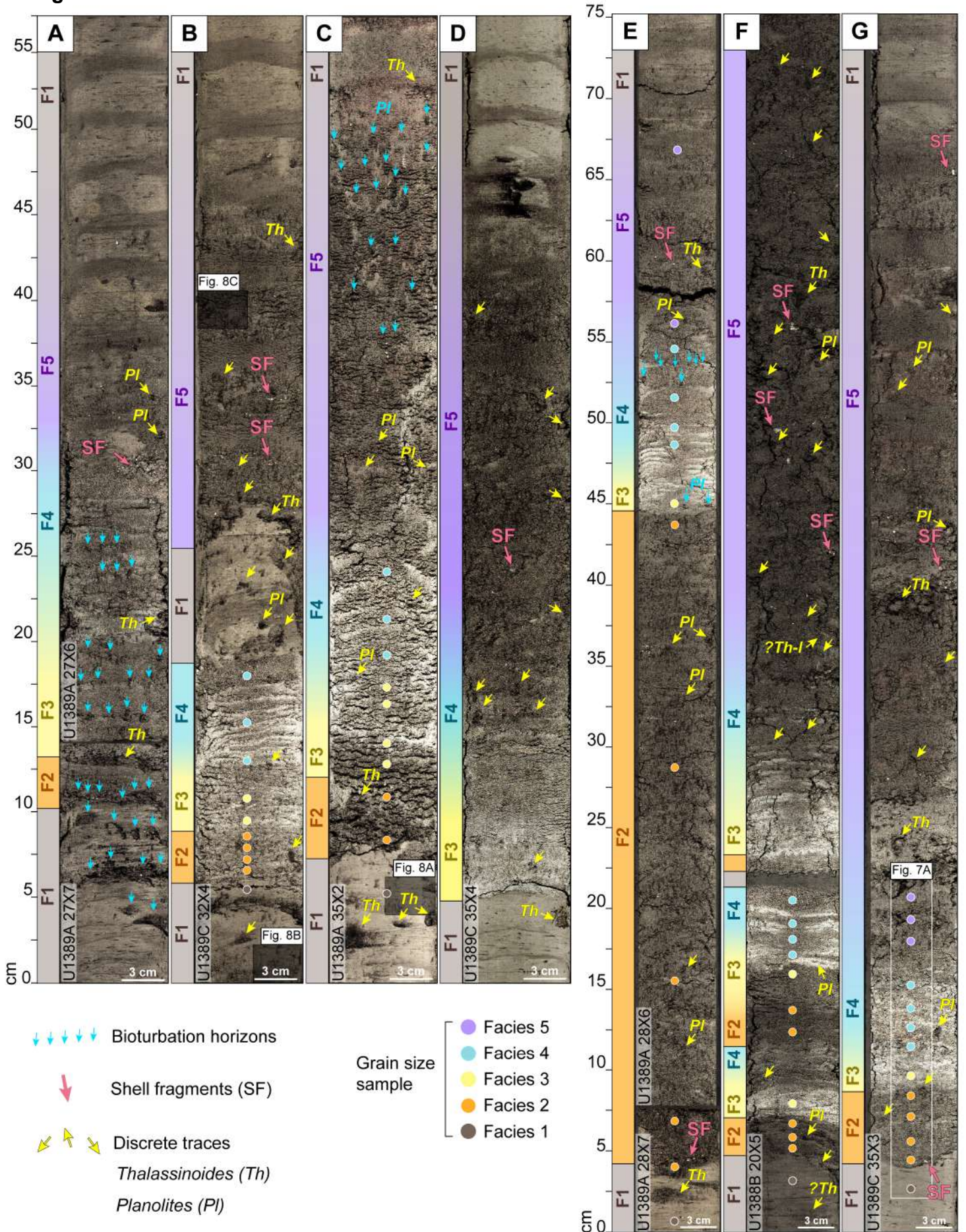


Figure 7.

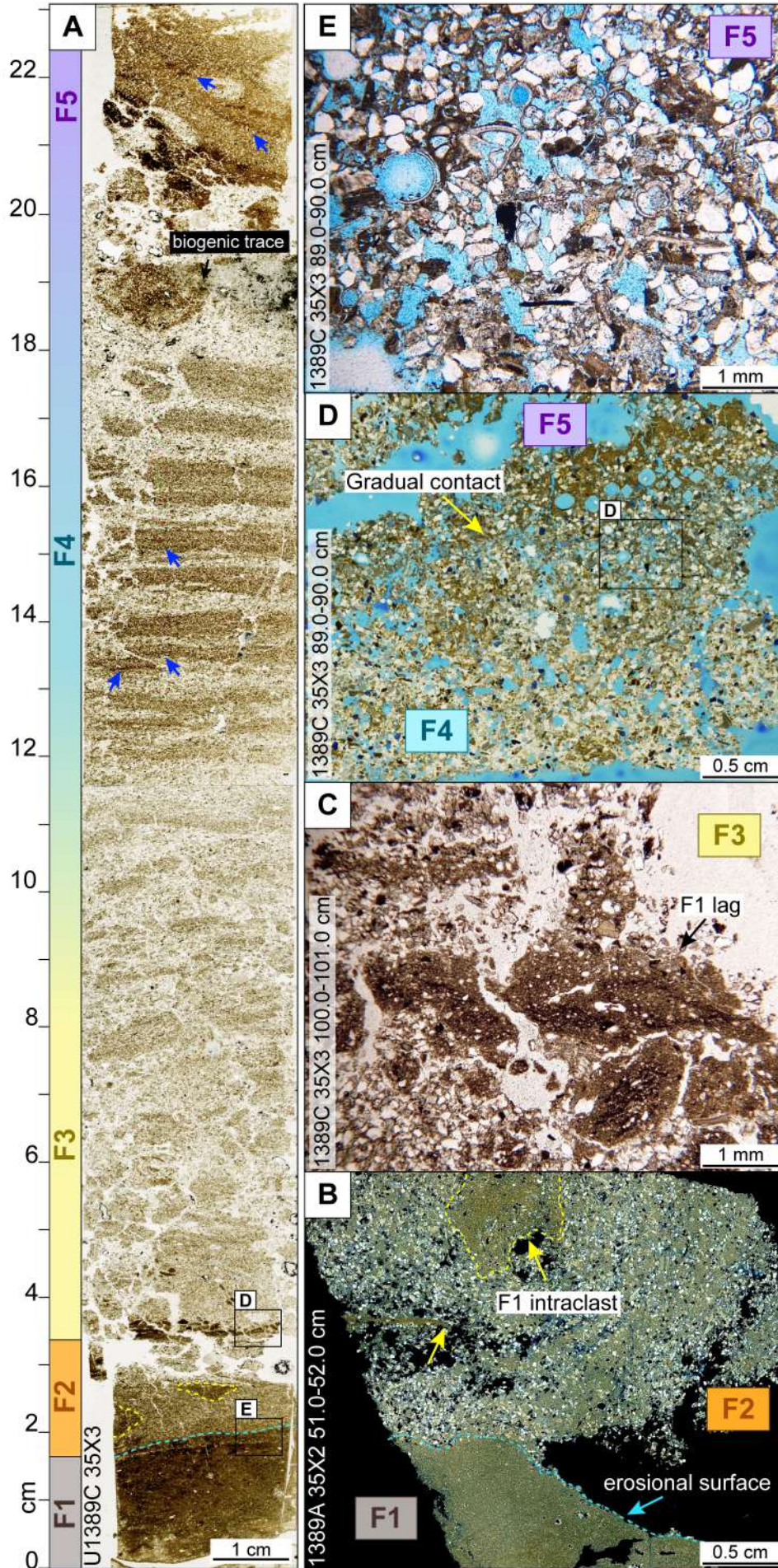


Figure 8.

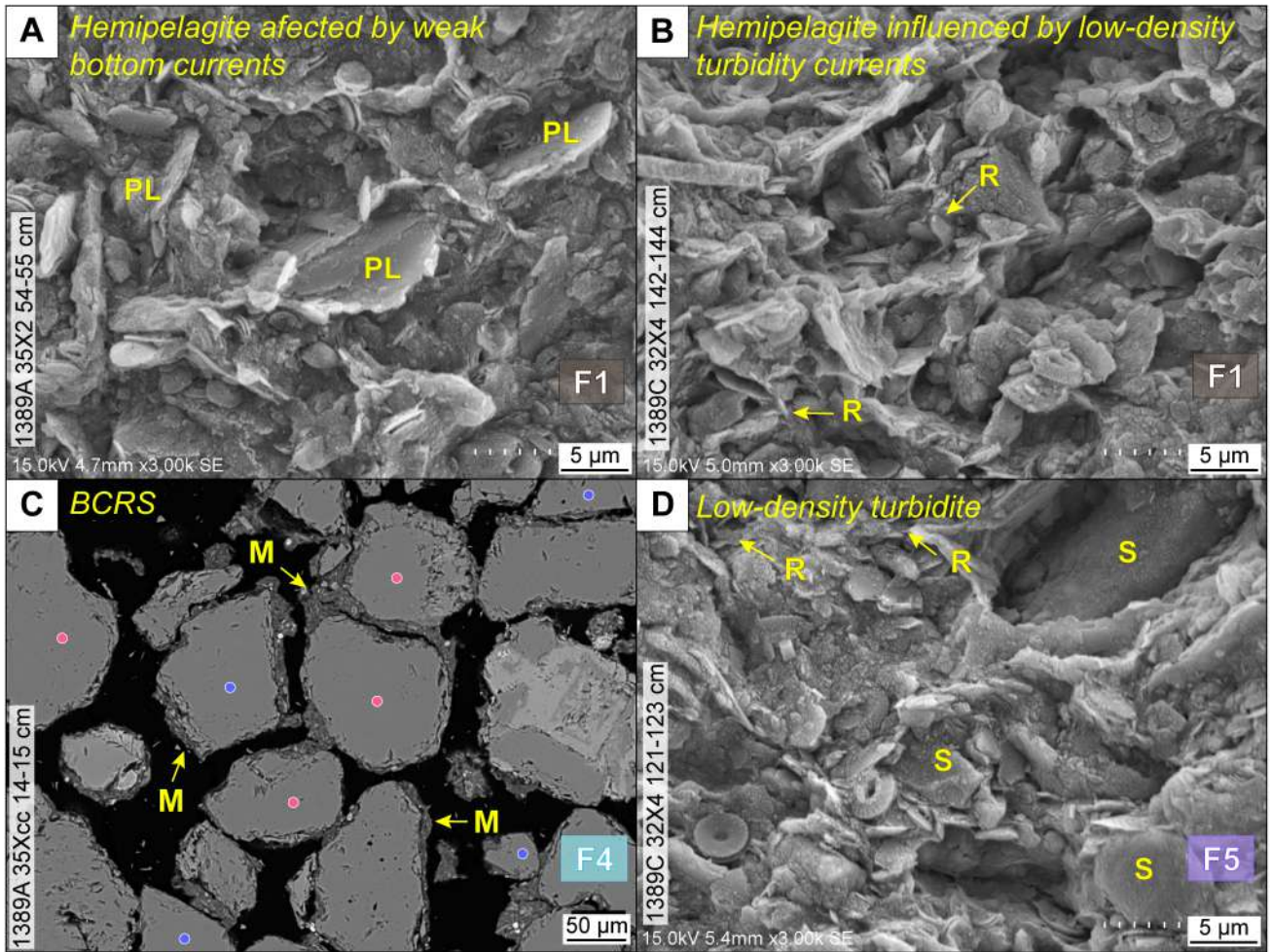
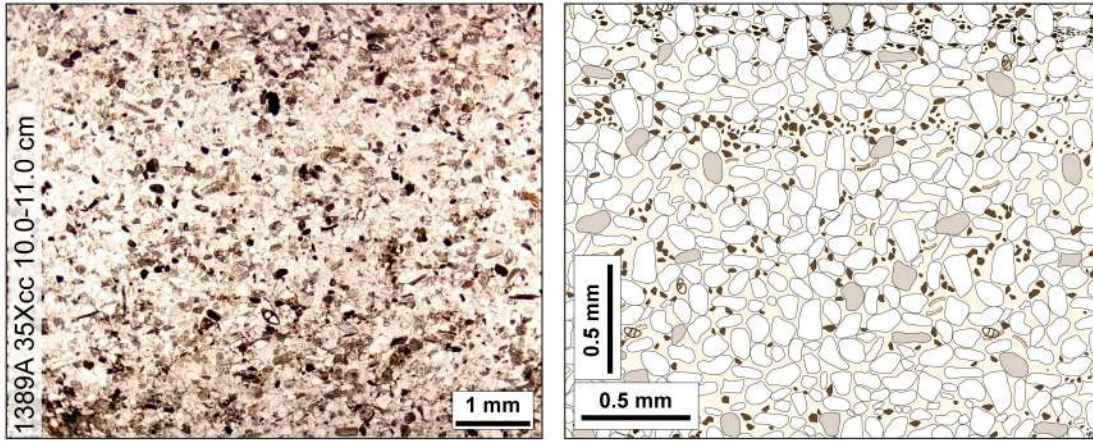
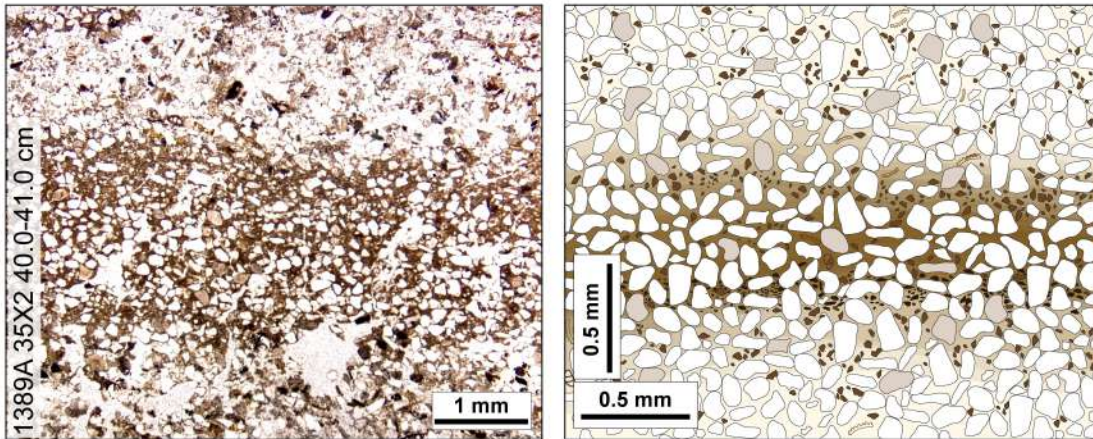


Figure 9.

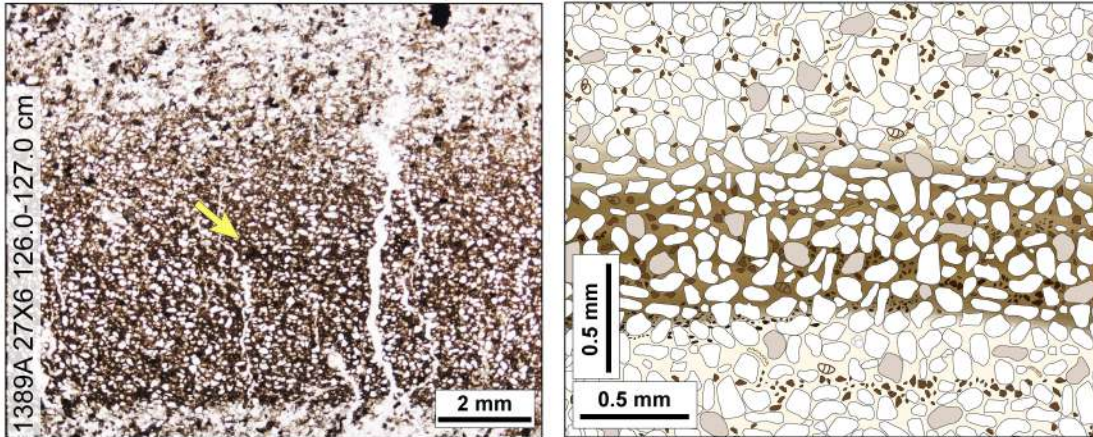
A. Winnowed laminae



B. Gradual mud-free mud-rich contact



C. Sharp base and transitional top mud-free mud-rich contact



D. Very-thin mud-free mud-rich intercalations

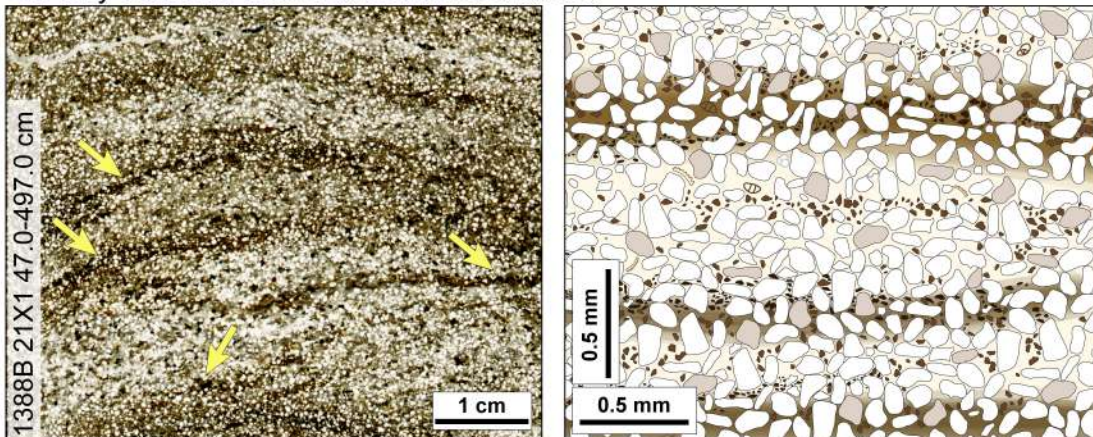


Figure 10.

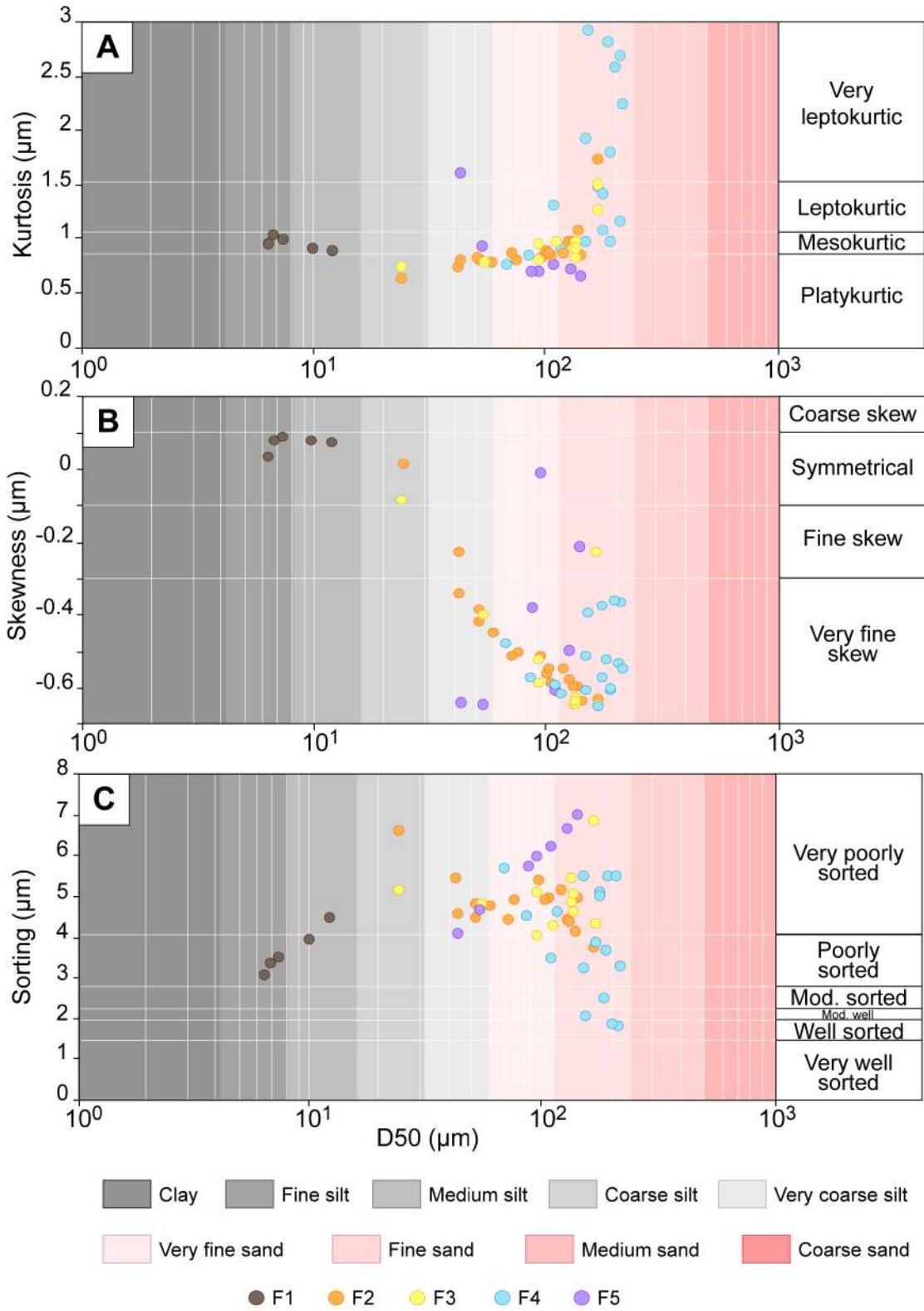
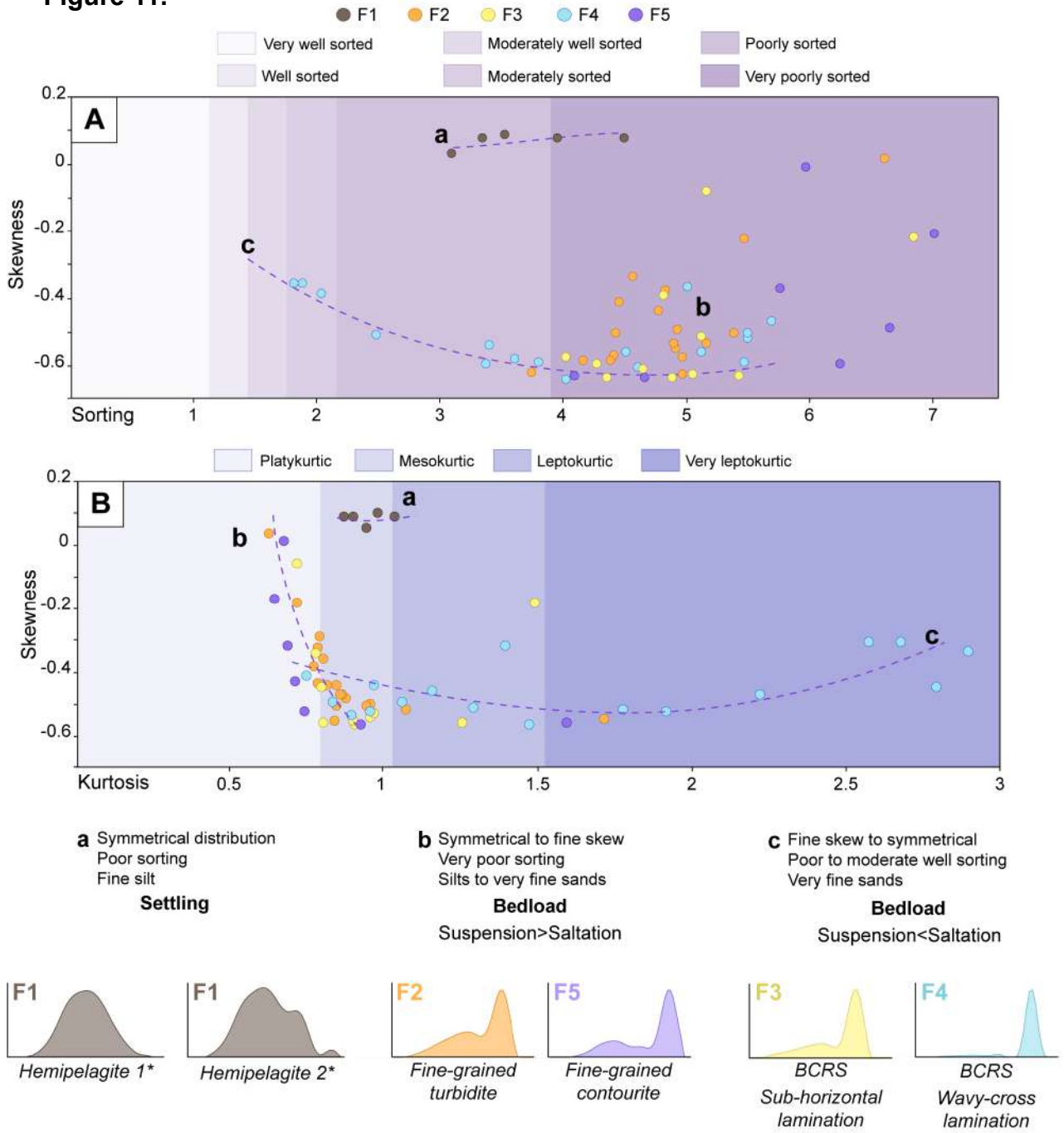


Figure 11.



* Hemipelagite 1. Settling dominated

* Hemipelagite 2. Affected by fine-grained suspension cloud or weak bottom currents

Figure 12.

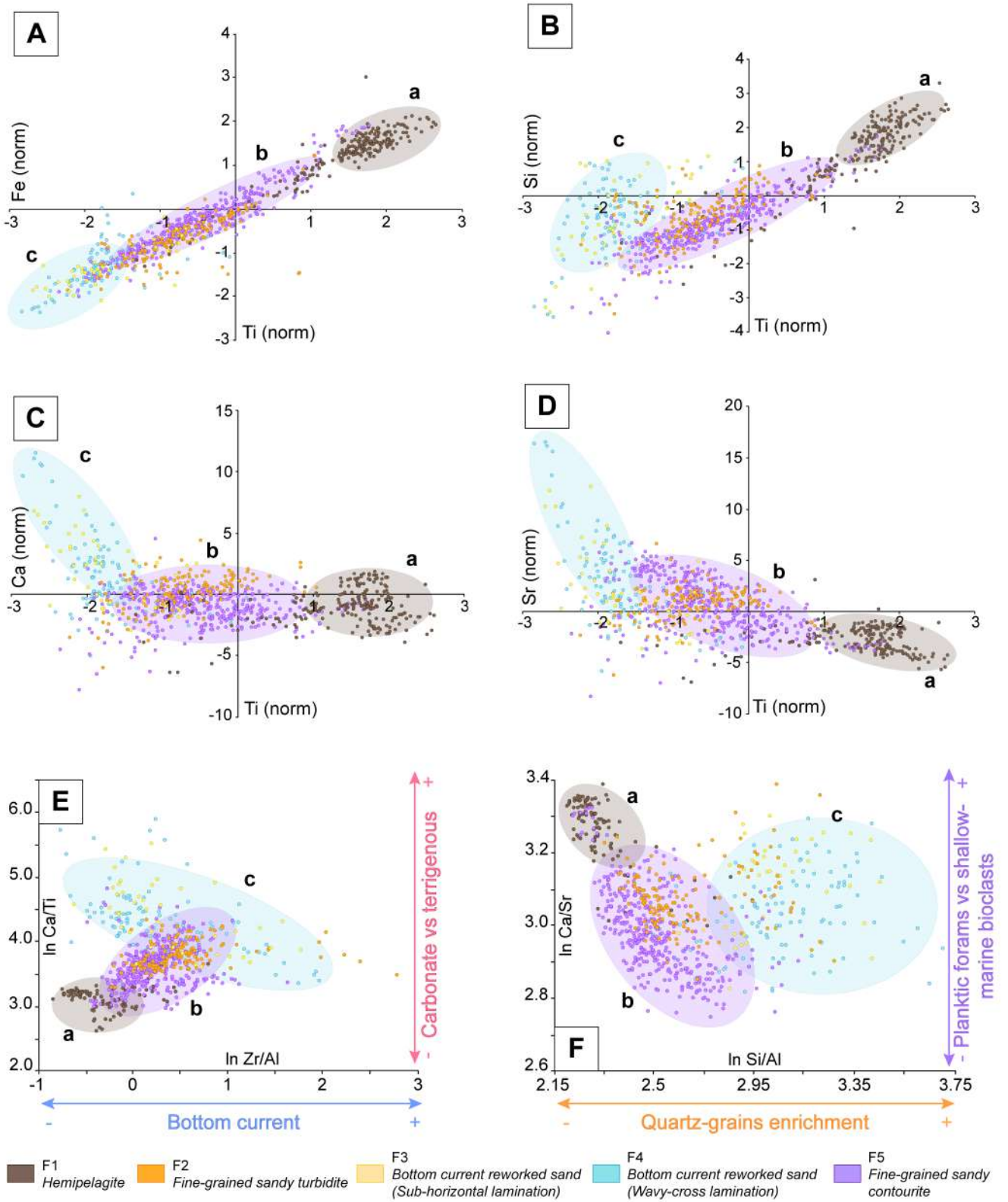


Figure 13.

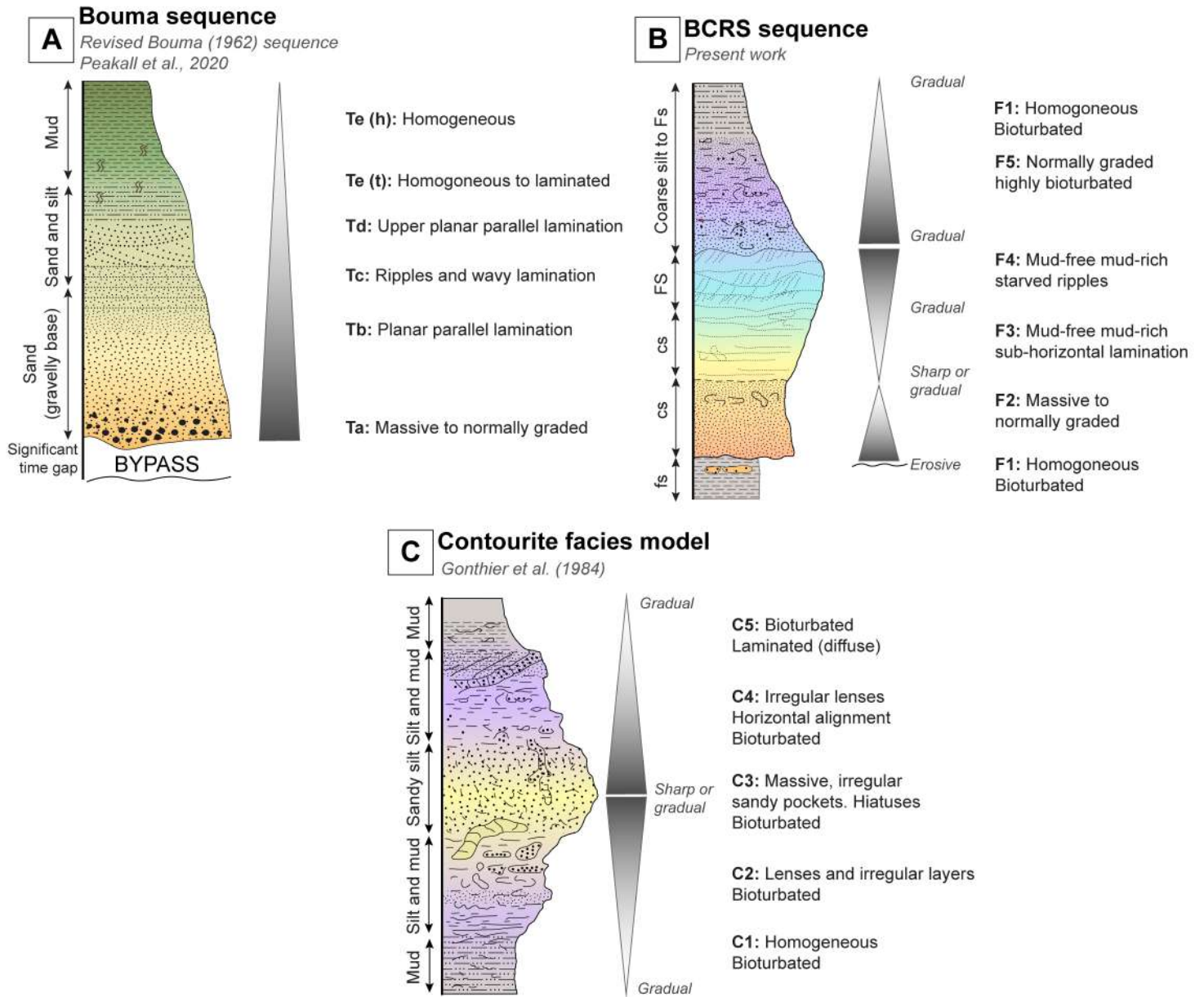
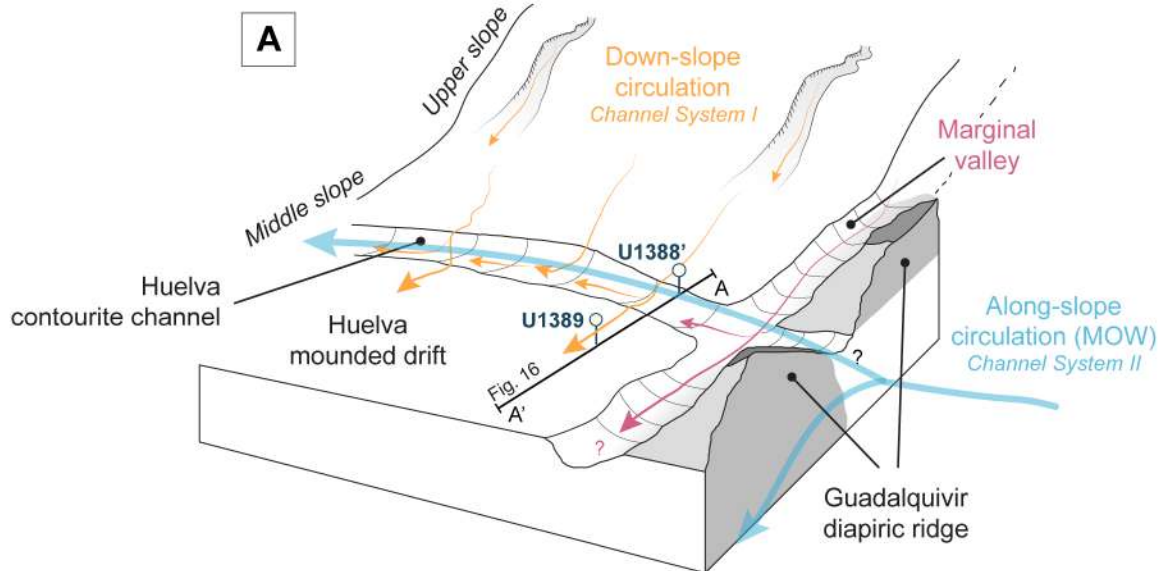
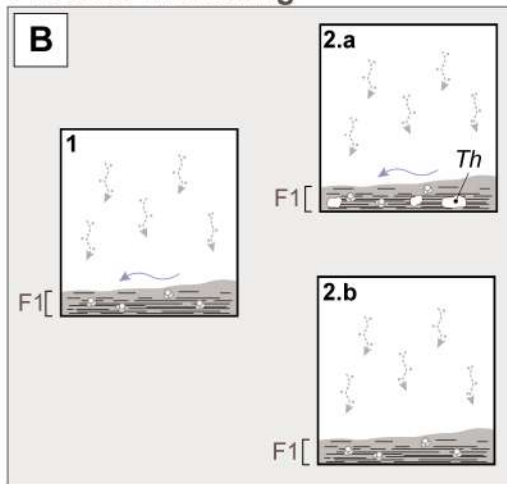


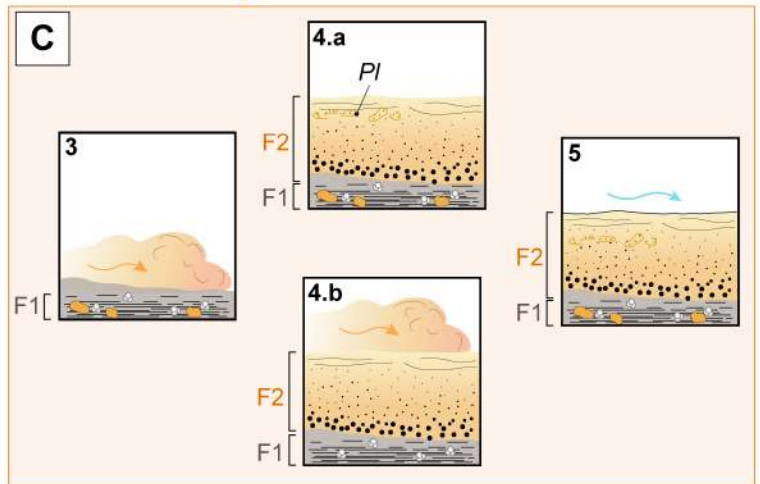
Figure. 14



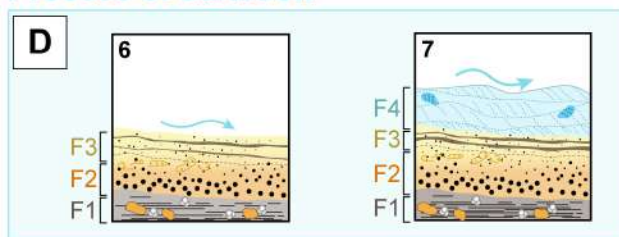
Process 1: Settling



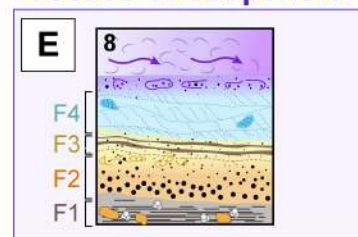
Process 2: Suspension



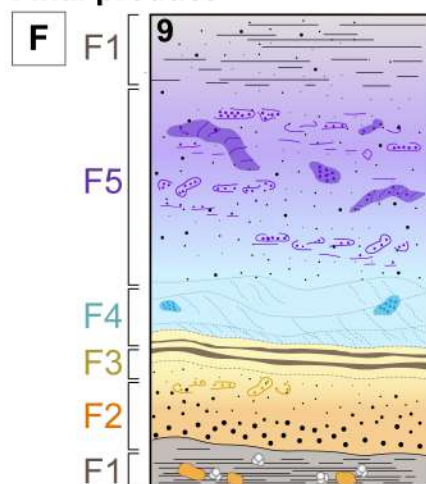
Process 3: Saltation



Process 4: Suspension



Final product

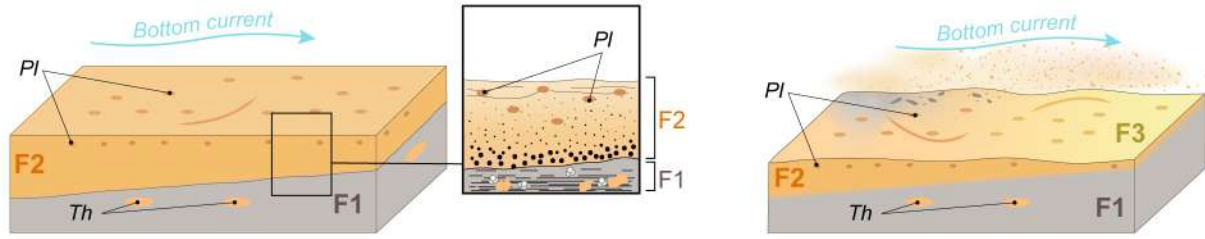


- Bottom-current activity
- Bottom-current activity
- Bottom-current activity
- Gravity-driven activity
- Settling
- Discrete traces
- Bioturbation horizons

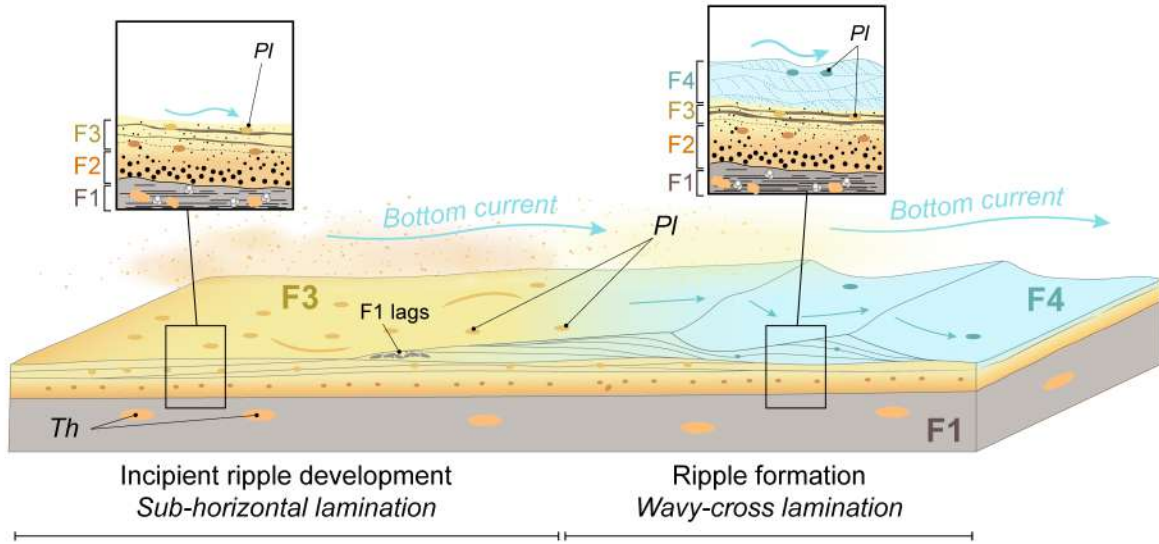
Figure. 15

A High shear stress due to mud content in F2

Shear stress gets less efficient due to winnowing of fine particles in F3



B Reworking and winnowing facilitates to form sandy equilibrium ripples with vigorous bottom currents



C Fine-grained sediment input from a suspended cloud (multiple events)

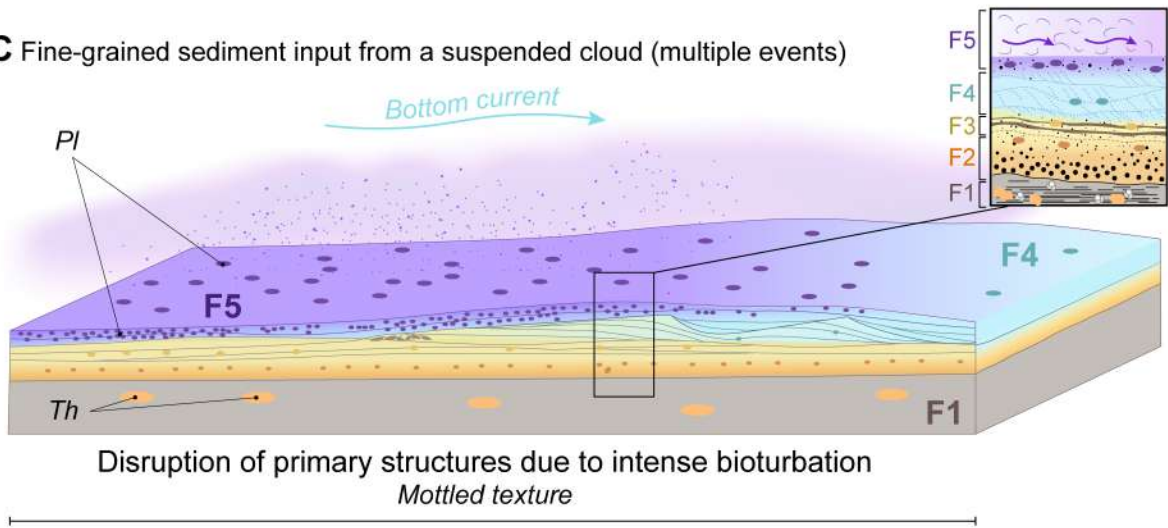


Figure. 16

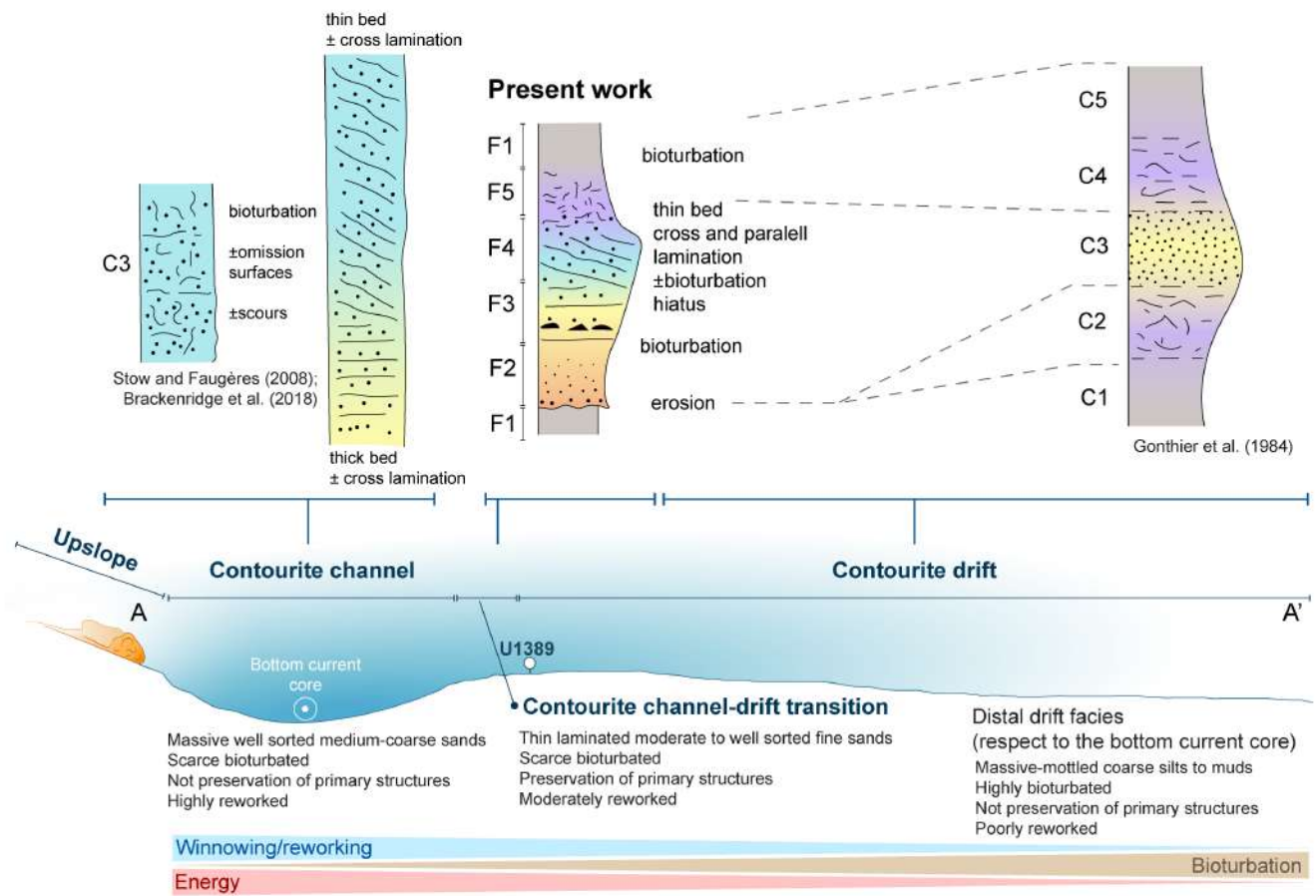


Figure. 17

